Linear systems formulation of scattering theory for rough surfaces with arbitrary incident and scattering angles

Andrey Krywonos, James E. Harvey,* and Narak Choi

The Center for Research and Education in Optics and Lasers (CREOL), P.O. Box 162700, 4000 Central Florida Boulevard, The University of Central Florida, Orlando, Florida 32826, USA
**Corresponding author: harvey@creol.ucf.edu*

Received February 9, 2011; accepted March 25, 2011;
posted April 8, 2011 (Doc. ID 142395); published May 19, 2011

Scattering effects from microtopographic surface roughness are merely nonparaxial diffraction phenomena resulting from random phase variations in the reflected or transmitted wavefront. Rayleigh–Rice, Beckmann–Kirchhoff. or Harvey–Shack surface scatter theories are commonly used to predict surface scatter effects. Smooth-surface and/or paraxial approximations have severely limited the range of applicability of each of the above theoretical treatments. A recent linear systems formulation of nonparaxial scalar diffraction theory applied to surface scatter phenomena resulted first in an empirically modified Beckmann–Kirchhoff surface scatter model, then a generalized Harvey–Shack theory that produces accurate results for rougher surfaces than the Rayleigh–Rice theory and for larger incident and scattered angles than the classical Beckmann–Kirchhoff and the original Harvey–Shack theories. These new developments simplify the analysis and understanding of nonintuitive scattering behavior from rough surfaces illuminated at arbitrary incident angles. © 2011 Optical Society of America

OCIS codes: 290.0290, 290.1483, 290.5825, 290.5835, 290.5880, 290.3200.

1. INTRODUCTION

Surface scatter phenomena continues to be an important issue in diverse areas of science and engineering in the 21st century. Two historical approaches, the Rayleigh–Rice (1951) [1,2] and the Beckmann–Kirchhoff (1963) [3] theories, are commonly used to predict surface scatter behavior. Harvey and Shack (1976) developed a linear systems formulation of surface scatter phenomena in which the scattering behavior is characterized by a surface transfer function [4,5]. This treatment provided insight and understanding not readily gleaned from the two previous theories.

The Rayleigh–Rice vector perturbation theory agrees well with experimental wide-angle scatter measurements from "smooth" ($4\pi\sigma_{\mathrm{rel}}\cos\theta_i/\lambda \ll 1$) surfaces for arbitrary incident and scattering angles. However, not all applications of interest satisfy the smooth-surface criterion. The Beckmann–Kirchhoff scattering theory is valid for rougher surfaces, but contains a paraxial (small-angle) assumption that limits its ability to accurately handle wide-angle scattering and large angles of incidence. The two most widely used surface scattering theories are thus complementary, but not all-inclusive; i.e., neither of them, nor the combination of them, adequately describes scattering behavior for moderately rough surfaces with large incident and scattering angles. Applications involving this general situation provided the motivation for developing the generalized surface scatter theory reported in this paper.

More than 10 years ago, an empirical modification of the Beckmann–Kirchhoff surface scatter theory was developed that appeared to satisfactorily combine the advantages of both the Rayleigh–Rice and the Beckmann–Kirchhoff theories without the disadvantages of either [6]. However, because it was empirically developed rather than theoretically derived, this work was only recently published in the archival literature [7]. In spite of that, the modified Beckmann–Kirchhoff surface scatter model has been evaluated, implemented, and referenced by researchers in the computer vision and computer animation fields who are less interested in rigorously solving the surface scatter problem than merely having a surface scatter model that results in the rendering of realistic surfaces, textures, objects, and scenes under a wide variety of illumination conditions [8–17].

The purpose of the current paper is to describe a linear systems formulation of a generalized surface scatter theory that allows the calculation of surface scatter behavior for moderately rough surfaces with arbitrary incident and scattered angles. We refer the reader to Section 1 of [7] for an exhaustive historical review of surface scatter theory. However, we do mention a critical survey of approximate scattering wave theories from random rough surfaces by Elfouhaily and Guerin in 2004 [18]. They attempted to classify and characterize more than 30 different approximate methods. These were all variants of the small perturbation method (Rayleigh–Rice), the Kirchhoff approach, or the so-called unified methods that tried to bridge the gap between the two. This exhaustive survey included 260 references. They concluded that "there does not seem to be a universal method that is to be preferred systematically. All methods present a compromise between versatility, simplicity, numerical efficiency, accuracy and robustness." Their final statement was "There is still room for improvement in the development of approximate scattering methods."

We also state in advance that surface scatter phenomena is merely a diffraction process, and [19–21] describe in detail the nonparaxial scalar diffraction theory that forms the basis of the generalized Harvey–Shack (GHS) surface scatter theory discussed in the body of this paper. Section 2 of [7] succinctly summarizes that nonparaxial scalar diffraction theory.

 © 2011 Optical Society of America

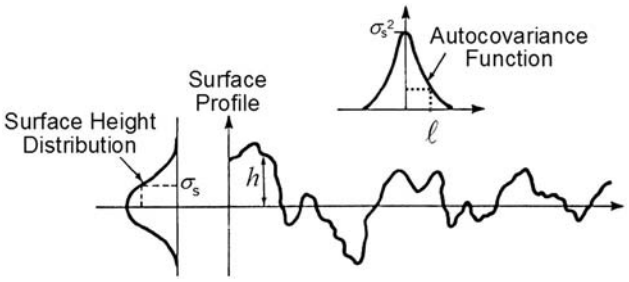

Fig. 1. Schematic diagram of a surface profile and its relevant statistical parameters.

2. SURFACE CHARACTERISTICS

The behavior of light scattered from randomly rough surfaces is dictated by the statistical surface characteristics. Consider the surface profile illustrated in Fig. 1. The surface has a zero mean with the surface height, h, illustrated as a function of position along a one-dimensional trace of finite length. Two relevant statistical surface characteristics are the surface height distribution function and the surface autocovariance (ACV) function. Fortunately, for many cases of interest, the surface heights are normally distributed (i.e., the surface height distribution function is Gaussian). The root-mean-square (rms) surface roughness, σ_s, is the standard deviation of that normal distribution.

Although it would be convenient (mathematically) if the surface ACV function were also Gaussian, in most instances that is not the case. Instead, the ACV function is material and process dependent. The ACV length, ℓ, is defined as the half-width of the ACV function at the $1/e$ height.

The surface power spectral density (PSD) function and the surface ACV function are Fourier transforms of each other. Note from Fig. 1 that the value of the surface ACV function at the origin is equal to the surface variance, σ_s^2. From the central ordinate theorem of Fourier transform theory, we therefore know that the volume under the two-dimensional surface PSD is also equal to the surface variance.

The surface PSD can be thought of as a plot of surface variance as a function of the spatial frequency of the surface irregularities. We can thus talk about several different relevant spatial-frequency regimes that have distinctly different effects upon image quality, as illustrated in Fig. 2.

The low-spatial-frequency regime ("figure" errors) gives rise to conventional wavefront aberrations. The high-spatial-frequency regime ("finish" errors or microroughness) produces wide-angle scattering effects that redistribute radiant energy from the image core into a broad scattered halo without substantially affecting the width of the image core. And the mid-spatial-frequency regime that spans the gap between the traditional figure and finish errors produces small-angle scatter that broadens or smears out the image core [22,23].

Historically, optical fabrication tolerances have been specified by placing a tolerance only upon the figure and finish errors. It has only recently become common practice to also specify a tolerance upon the mid-spatial-frequency surface irregularities.

The astronomer's classical definition of resolution has been the full width at half-maximum (FWHM) of the point spread function (PSF). For bright point sources, this image quality criterion is quite insensitive to wide-angle scatter resulting from high-spatial-frequency microroughness since the width of the image core is not significantly broadened. However, for faint point sources, the wide-angle scattered halo causes severe signal-to-noise problems and a substantial loss of image contrast. The small-angle scatter produced by the mid-spatial-frequency surface irregularities does broaden the image core and, therefore, causes a significant decrease in resolution (larger FWHM). It is thus imperative that optical fabrication tolerances be specified (and measured) over the entire range of relevant spatial frequencies.

A uniformly rough surface is one whose roughness is homogeneous and isotropic; i.e., the surface height distribution function and the ACV function do not change with location or orientation of the (finite) measured surface profile. For

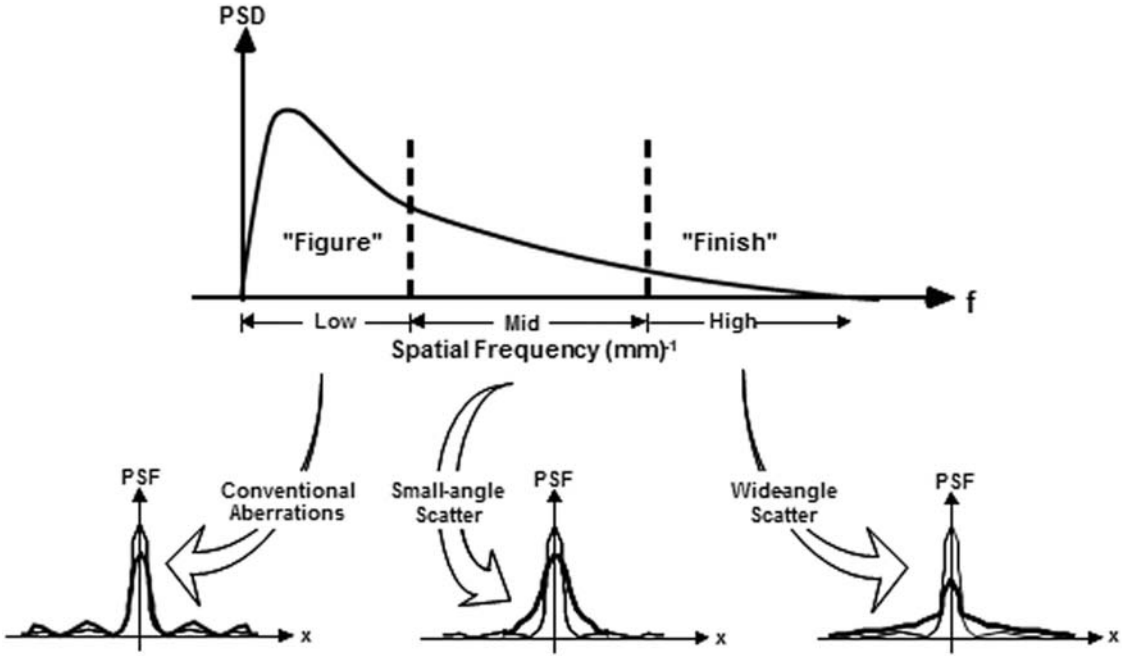

Fig. 2. Different spatial-frequency regimes and their resulting effects upon image quality.

such a surface, the PSD is a two-dimensional, rotationally symmetric function. Church has reported upon the fractal nature of many surface finishes, thus suggesting that the surface PSD can be modeled as exhibiting an inverse power law behavior [24].

It is important to recognize that the relevant surface roughness is not an intrinsic surface characteristic, but a band-limited quantity that depends upon the wavelength and incident angle [2,25]. For normal incidence, those spatial frequencies greater than $1/\lambda$ produce evanescent (imaginary) waves that do not result in radiant power being scattered from the specular beam; i.e., spatial frequencies greater than $1/\lambda$ are completely irrelevant with regard to scattered light. For an arbitrary incident angle, θ_i, the two-dimensional boundary of the appropriate band-limited portion of the surface PSD is illustrated in Fig. 3(a), i.e., a circle of radius $1/\lambda$ whose center is shifted to a spatial frequency given by [26]

$$f_o = \frac{\sin\theta_o}{\lambda}, \qquad \theta_o = -\theta_i. \tag{1}$$

The corresponding relevant roughness, σ_{rel}, is given by the square root of the volume under the relevant portion of the surface PSD illustrated in Fig. 3(b). It is thus calculated by the following integral [26]:

$$\sigma_{\mathrm{rel}}(\lambda,\theta_i) = \sqrt{\int_{-1/\lambda+f_o}^{1/\lambda+f_o} \int_{-\sqrt{1/\lambda^2-(f_x-f_o)^2}}^{\sqrt{1/\lambda^2-(f_x-f_o)^2}} \mathrm{PSD}(f_x,f_y)\,df_x\,df_y}. \tag{2}$$

It is the above relevant roughness, σ_{rel}, that determines the fraction of the total reflected light contained in the specular beam and the associated scattering function. For normal incidence, the relevant roughness expressed by Eq. (2) simplifies to

$$\sigma_{\mathrm{rel}}(\lambda) = \sqrt{2\pi \int_{f=0}^{1/\lambda} \mathrm{PSD}(f) f\,df}. \tag{3}$$

For some applications there is a nonzero low-spatial-frequency band limit, $1/L$, where L represents an inherent measurement bandwidth limit [27–29].

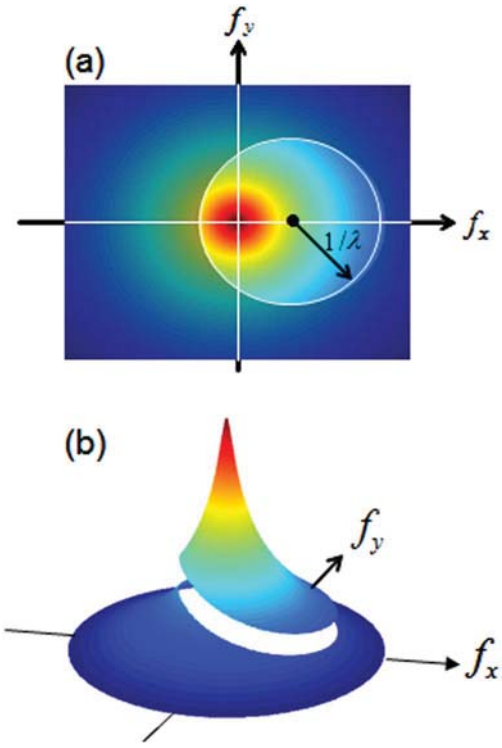

Fig. 3. (Color online) (a) Illustration of the two-dimensional boundary of the appropriate band-limited portion of the surface PSD for an arbitrary incident angle, θ_i. (b) Illustration of the relevant portion of the surface PSD, whose integral yields the square of the relevant rms surface roughness.

3. LINEAR SYSTEMS FORMULATION OF SURFACE SCATTER THEORY

A linear systems formulation of surface scatter phenomena, utilizing the same Fourier techniques that have proven so successful in the area of image formation, shows great promise for not only simplifying the actual calculation of scattered light behavior, but for providing new insight and understanding concerning a topic that is generally perceived as being very complicated. In this section, we present the evolution of the current GHS surface scatter theory from its origin in [4].

A. Original Harvey–Shack Surface Scatter Theory

Harvey and Shack (1976) first developed a linear systems formulation of surface scatter phenomena in which the scattering behavior is characterized by a surface transfer function [4,5]:

$$H_s(\hat{x},\hat{y}) = \exp\{-(4\pi\hat{\sigma}_s)^2[1 - C_s(\hat{x},\hat{y})/\sigma_s^2]\}, \tag{4}$$

where σ_s is the rms surface roughness (the concept of a band-limited relevant roughness had not yet been considered) and $C_s(\hat{x},\hat{y})$ is the surface ACV function. The scattered light distribution, called an angle spread function (ASF) in analogy with the PSF of imaging systems, is given by the Fourier transform of this surface transfer function.

The surface transfer function of Eq. (4) can also be written in the form

$$H(\hat{x},\hat{y}) = A + BG(\hat{x},\hat{y}), \tag{5}$$

where

$$A = \exp[-(4\pi\hat{\sigma}_s)^2], \tag{6}$$

$$B = 1 - \exp[-(4\pi\hat{\sigma}_s)^2], \tag{7}$$

are the fraction of the total reflected radiant power contained in the specular and the scattered components, respectively, and

$$G(\hat{x},\hat{y}) = \frac{\exp[(4\pi)^2 C_s(\hat{x},\hat{y})] - 1}{\exp(4\pi\hat{\sigma}_s)^2 - 1}. \tag{8}$$

From Eq. (5), we see that the surface transfer function can be written as the sum of two separate components. The ASF is therefore expressed as the sum of the Fourier transforms of the two components making up the surface transfer function:

$$\mathrm{ASF}(\alpha,\beta) = \mathsf{F}\{H(\hat{x},\hat{y})\} = A\delta(\alpha,\beta) + S(\alpha,\beta), \tag{9}$$

where the scattering function, $S(\alpha,\beta)$, is given by

$$S(\alpha,\beta) = B\mathsf{F}\{G(\hat{x},\hat{y})\}. \tag{10}$$

Therefore, the scattering surface reflects an incident beam of light as a specularly reflected beam (the delta function) of diminished intensity surrounded by a halo of scattered light.

The ASF, and the corresponding scattering function are scattered radiance functions, which is consistent with the fact that the bidirectional reflectance distribution function (BRDF) was defined by Nicodemus in 1970 as the reflected (or scattered) radiance divided by the incident irradiance [30]:

$$\mathrm{BRDF} = f(\theta_i,\phi_i,\theta_s,\phi_s) = \frac{dL(\theta_i,\phi_i,\theta_s,\phi_s)}{dE(\theta_i,\phi_i)}. \tag{11}$$

The four-dimensional BRDF is made up of a superposition of the above two-dimensional ASFs, one for every possible angle of incidence:

$$\mathrm{BRDF}(\theta_i,\phi_i,\theta_s,\phi_s) = \sum_{\theta_i,\phi_i} R\mathrm{ASF}(\alpha,\beta). \tag{12}$$

Here R is the scalar reflectance of the scattering surface. Alternatively, for a given angle of incidence, the BRDF is related to the ASF by

$$\mathrm{BRDF}(\theta_i,\phi_i,\theta_s,\phi_s)|_{\theta_i,\phi_i} = R\mathrm{ASF}(\alpha,\beta). \tag{13}$$

Starting with the assumption that the two-dimensional surface height variation constitutes a Gaussian random process that is homogeneous and isotropic, Eq. (4) was derived using the same procedure as that used in image evaluation; i.e., the surface transfer function is defined as the normalized autocorrelation of the complex pupil function. In addition to [4], this derivation has been repeated in [31,32].

Note that a scaled coordinate system has been used in which the spatial variables are normalized by the wavelength of the light ($\hat{x} = x/\lambda$, $\hat{y} = y/\lambda$, etc.). The reciprocal variables α and β are thus the direction cosines of the propagation vectors of the angular spectrum of plane waves discussed by Ratcliff [33], Goodman [34], and Gaskill [35]. These direction cosines α, β, and γ are related to the angular variables θ and ϕ in conventional spherical coordinates by the following expressions [36]:

$$\alpha = \sin\theta\cos\phi, \qquad \beta = \sin\theta\sin\phi, \qquad \gamma = \cos\theta. \tag{14}$$

Although there was no explicit smooth-surface approximation in this original Harvey–Shack (OHS) surface scatter theory, the derivation of Eq. (4) did suffer from the same paraxial limitations as the classical Beckmann–Kirchhoff theory. Within those limitations, for a broad class of scattering surfaces, including optical surfaces polished with conventional abrasive grinding and polishing techniques on ordinary glassy amorphous materials, the ASF exhibits shift-invariant behavior in direction cosine space with respect to incident angle [4,5,37]. This led to a modest following among the radiometric community of BRDF curves plotted in the Harvey–Shack $\beta - \beta_o$ format. Breault made extensive use of this format in building a catalog of BRDF data from various materials and surfaces for use in his APART baffle design program [38]. Today the ASAP, Trace-Pro, ZEMAX, and FRED codes all use some form of the Harvey–Shack BRDF model [39–42], and the Optical Society of America Optics Classification and Indexing Scheme includes a code for Harvey scattering [43].

Also, if one does make the smooth-surface approximation, the quantity $G(\hat{x},\hat{y})$ reduces to the normalized surface ACV function, $C_s(\hat{x},\hat{y})/\sigma_s^2$, and the scattering function becomes proportional to the surface PSD function. This is similar to the result predicted by the classical Rayleigh–Rice theory as discussed in Subsection 4.C [1,25].

B. Modified Harvey–Shack Surface Scatter Theory

The above transfer function characterization of scattering surfaces was modified in the 1980s to include grazing incidence effects in x-ray telescopes, and mid-spatial-frequency surface errors that span the gap between figure and finish errors [44]. This allowed an understanding of image degradation due to scattering effects from residual optical fabrication errors on NASA's Chandra Observatory and NOAA's Solar X-ray Imager [45,46].

Figure 4 shows a ray incident upon a scattering surface at an arbitrary angle of incidence θ_i. The optical path difference (OPD) experienced by a ray reflected from the surface in the specular ($\theta_o = -\theta_i$) direction is given by

$$\mathrm{OPD} = (\gamma_i + \gamma_o)h(\hat{x},\hat{y}) = 2\gamma_i h(\hat{x},\hat{y}), \tag{15}$$

where $\gamma_i = \cos\theta_i$ and $\gamma_o = \cos\theta_o$. The corresponding phase variation is given by

$$\phi(\hat{x},\hat{y}) = (2\pi/\lambda)\mathrm{OPD} = 4\pi\gamma_i\hat{h}(\hat{x},\hat{y}). \tag{16}$$

Provided that the scattering angles are small relative to the angle of specular reflection, the phase function of Eq. (16) describes the phase variations introduced upon reflection from a scattering surface for a wavefront incident at an arbitrary angle.

Krywonos showed that the surface transfer function for an arbitrary incident angle (assuming small-angle scattering) can be expressed as [32]

$$H_s(\hat{x},\hat{y};\gamma_i) = \exp\{-(4\pi\gamma_i\hat{\sigma}_{\mathrm{ref}})^2[1 - C_s(\hat{x},\hat{y})/\sigma_s^2]\}. \tag{17}$$

This can again be written in the form

$$H_s(\hat{x},\hat{y};\gamma_i) = A(\gamma_i) + B(\gamma_i)G(\hat{x},\hat{y};\gamma_i), \tag{18}$$

where

$$A(\gamma_i) = \exp[-(4\pi\gamma_i\hat{\sigma}_{\mathrm{rel}})^2], \qquad B(\gamma_i) = 1 - \exp[-(4\pi\gamma_i\hat{\sigma}_{\mathrm{rel}})^2], \tag{19}$$

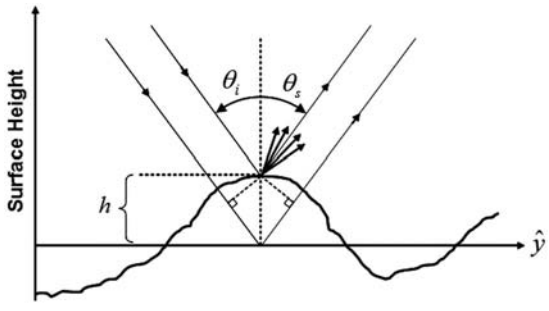

Fig. 4. Illustration of the OPD for a specularly reflected ray.

$$G(\hat{x},\hat{y};\gamma_i)=\frac{\exp[(4\pi\gamma_i)^2C_s(\hat{x},\hat{y})]-1}{\exp[(4\pi\gamma_i\hat{\sigma}_{\mathrm{rel}})^2]-1}. \quad (20)$$

In Eq. (17) we have used the relevant surface roughness, σ_{rel}, introduced in Eq. (2) since spatial frequencies lying outside of the band-limited portion of the surface PSD do not contribute to the scattered radiation [47]. The surface ACV function is divided by the total, or intrinsic, roughness, σ_s, as its purpose is to normalize the height of the surface ACV function to unity. Equation (19) expresses the fraction of the total reflected radiant power contained in the specular beam, and in the scattered component, after reflection from a single moderately rough surface [48–50,3,25]. These relationships are very important to the following discussion. We thus bring to the attention of the reader the brief historical perspective of these relationships presented on p. 51 of [50].

A wavefront incident on the scattering surface at an angle θ_i introduces a linear phase variation across the pupil. Since the ASF is given by the Fourier transform of the surface transfer function, we can apply the shift theorem of Fourier transform theory to Eq. (18) and obtain

$$\begin{aligned}\mathrm{ASF}(\alpha,\beta-\beta_o;\gamma_i)&=\mathsf{F}\{H_s(\hat{x},\hat{y};\gamma_i)\exp(-i2\pi\hat{y}\beta_o)\}\\&=A(\gamma_i)\delta(\alpha,\beta-\beta_o)+S(\alpha,\beta-\beta_o;\gamma_i),\end{aligned} \quad (21)$$

where

$$\begin{aligned}S(\alpha,\beta-\beta_o;\gamma_i)&=B(\gamma_i)\mathsf{F}\{G(\hat{x},\hat{y};\gamma_i)\exp(-i2\pi\hat{y}\beta_o)\},\\ \beta_o&=-\beta_i.\end{aligned} \quad (22)$$

This is the sum of a delta function at the location of the specular direction surrounded by a scattering function, S, where the fraction of the total reflected radiant power in the specular beam is given by $A(\gamma_i)$, and the fraction of total reflected radiant power in the scattering function, i.e., the total integrated scatter (TIS), is given by $B(\gamma_i)$. From Eq. (19), clearly $A(\gamma_i)+B(\gamma_i)=1$ and the ASF has unit volume. If the volume of the scattering function, S, calculated by integrating Eq. (22) is not equal to TIS, the scattering function will need to be renormalized in accordance with the nonparaxial scalar diffraction theory described in [19–21]. The renormalization constant, $K(\gamma_i)$, for the scattering function is given by the following expression:

$$K(\gamma_i)=B(\gamma_i)\left(\int_{\alpha=-1}^{1}\int_{\beta=-\sqrt{1-\alpha^2}}^{\sqrt{1-\alpha^2}}S(\alpha,\beta-\beta_o;\gamma_i)d\alpha d\beta\right)^{-1}, \quad (23)$$

and only differs from unity for large incident and scattered angles where the scattered radiance distribution function extends beyond the unit circle in direction cosine space (i.e., only if evanescent waves are produced) [19].

Recall that the ASF is a radiance function of unit volume. We can convert the ASF to radiant intensity by multiplying by the total reflected radiant power and Lambert's cosine function:

$$I(\alpha,\beta-\beta_o;\gamma_i)=RP_i\mathrm{ASF}(\alpha,\beta-\beta_o;\gamma_i)\cos\theta_s. \quad (24)$$

Clearly the surface scatter process is no longer shift invariant with respect to incident angle, as reported in [4], since Eq. (17) can be interpreted as a one-parameter family of surface transfer functions; i.e., a different surface transfer function is required for each incident angle. This is analogous to imaging in the presence of field-dependent aberrations, where a different optical transfer function is required for each field angle.

C. Generalized Harvey–Shack Surface Scatter Theory

The modified version of the Harvey–Shack (MHS) theory is a significant improvement over the OHS theory, especially for large incident angles. However, the restriction of small scattering angles is still very limiting. Furthermore, the OHS and the MHS surface scatter theories were restricted to mirror surfaces, and did not include the more general situation of scattering from a random rough interface between two media with arbitrary refractive indices.

Figure 5 illustrates the OPD introduced when an incident ray at an arbitrary angle of incidence, θ_i, is scattered at an arbitrary angle, θ_s, by a moderately rough interface between two media with arbitrary refractive indices [26].

The OPD introduced by scattering from such an interface can be written as

$$\mathrm{OPD}(\hat{x},\hat{y})=-(n_1\cos\theta_i-n_2\cos\theta_s)h(\hat{x},\hat{y}), \quad (25)$$

where n_1 and n_2 are the refractive indices of the media before and after the interface, respectively.

The phase variation introduced for light scattered at an arbitrary angle is thus given by the following expression:

$$\phi(\hat{x},\hat{y};\gamma_i,\gamma_s)=(2\pi/\lambda)\mathrm{OPD}=-2\pi(n_1\cos\theta_i\mp n_2\cos\theta_s)\hat{h}(\hat{x},\hat{y}). \quad (26)$$

Because of the well-known π phase change experienced by an electromagnetic wave upon external reflection ($n_2\geq n_1$) from the boundary between two dielectric media [51], the minus sign is used when $n_2\leq n_1$ and the plus sign is used when $n_2\geq n_1$.

Returning to the derivation of the OHS theory [4,31,32], we find that the following two-parameter family of surface transfer functions is required to characterize the scattering process for arbitrary incident and scattering angles [26]:

$$H_s(\hat{x},\hat{y};\gamma_i,\gamma_s)=\exp\{-[2\pi\hat{\sigma}_{\mathrm{rel}}(n_1\gamma_i\mp n_2\gamma_s)]^2[1-C_s(\hat{x},\hat{y})/\sigma_s^2]\}, \quad (27)$$

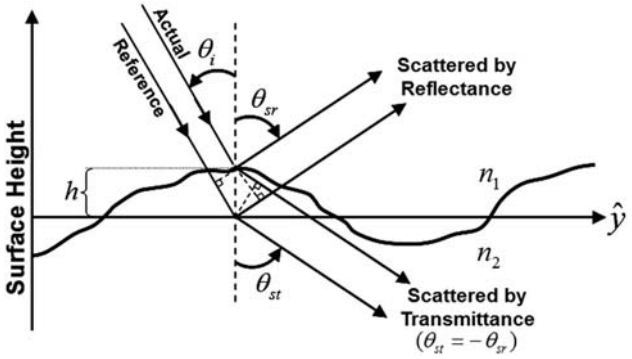

Fig. 5. Illustration of both forward (transmitted) and backward (reflected) scattering from a moderately rough interface between two media with arbitrary refractive indices.

where

$$\gamma_i = \cos\theta_i, \qquad \gamma_s = \cos\theta_s. \tag{28}$$

This general expression for the surface transfer function may be used to model either reflective or transmissive scatter, the latter being of interest, for example, in calculating the increased efficiency of thin-film photovoltaic silicon solar cells by utilizing enhanced roughness on the TCO–Si interface [52–54]. However, the discussion in this paper will be restricted to applications of scattering from mirror surfaces, i.e., $n_2 = -n_1$. If the mirror is immersed in air (or vacuum), $n_1 = 1$ and Eq. (27) can be written as

$$H_s(\hat{x},\hat{y};\gamma_i,\gamma_s) = \exp\{-[2\pi\hat{\sigma}_{\mathrm{rel}}(\gamma_i+\gamma_s)]^2[1 - C_s(\hat{x},\hat{y})/\sigma_s^2]\}. \tag{29}$$

A separate surface transfer function is thus required for each incident angle and each scattering angle. Note that we are again representing the effective rms surface roughness with the band-limited relevant rms roughness, $\hat{\sigma}_{\mathrm{rel}}$, defined previously in Eq. (2). The σ_s^2 at the end of Eqs. (27) and (29) remains as the square of the total, or intrinsic, surface roughness, as its purpose is to merely normalize the surface ACV function to unit height.

Since the Fourier transform of the above surface transfer function yields the ASF for normal incidence, we can again invoke the shift theorem of Fourier transform theory and express the scattered radiance distribution for an arbitrary incident angle, $\theta_i = -\theta_o$, by

$$\mathrm{ASF}(\alpha_s,\beta_s;\gamma_i,\gamma_s) = \mathsf{F}\{H_s(\hat{x},\hat{y};\gamma_i,\gamma_s)\exp(-i2\pi\beta_o\hat{y})\}|_{\alpha=\alpha_s,\beta=\beta_s}. \tag{30}$$

Equation (30) corresponds to the scattered radiance in the α_s, β_s direction. The direction cosines α_s and β_s are related to γ_s by

$$\gamma_s = \sqrt{1-\alpha_s^2-\beta_s^2}. \tag{31}$$

The surface transfer function can again be written in the form

$$H_s(\hat{x},\hat{y};\gamma_i,\gamma_s) = A(\gamma_i,\gamma_s) + B(\gamma_i,\gamma_s)G(\hat{x},\hat{y};\gamma_i,\gamma_s), \tag{32}$$

where

$$A(\gamma_i,\gamma_s) = \exp\{-[2\pi(\gamma_i+\gamma_s)\hat{\sigma}_{\mathrm{rel}}]^2\}, \tag{33}$$

$$B(\gamma_i,\gamma_s) = 1 - \exp\{-[2\pi(\gamma_i+\gamma_s)\hat{\sigma}_{\mathrm{rel}}]^2\}, \tag{34}$$

$$G(\hat{x},\hat{y};\gamma_i,\gamma_s) = \frac{\exp\left\{[2\pi(\gamma_i+\gamma_s)]^2\frac{\sigma_{\mathrm{rel}}^2}{\sigma_s^2}C_s(\hat{x},\hat{y})\right\} - 1}{\exp[2\pi(\gamma_i+\gamma_s)]^2\hat{\sigma}_{\mathrm{rel}}^2 - 1}. \tag{35}$$

The ASF can thus be written as the sum of a shifted δ function (specularly reflected beam) and an associated scattering function, $S(\alpha,\beta;\gamma_i,\gamma_s)$:

$$\mathrm{ASF}(\alpha_s,\beta_s;\gamma_i,\gamma_s) = [A(\gamma_i,\gamma_s)\delta(\alpha,\beta-\beta_o) + S(\alpha,\beta;\gamma_i,\gamma_s)]|_{\alpha=\alpha_s,\beta=\beta_s}, \tag{36}$$

where

$$S(\alpha,\beta;\gamma_i,\gamma_s) = B(\gamma_i,\gamma_s)\mathsf{F}\{G(\hat{x},\hat{y};\gamma_i,\gamma_s)\exp(-i2\pi\beta_o\hat{y})\}. \tag{37}$$

Equations (29) and (37) indicate that, for a given incident angle, a different Fourier transform needs to be performed for each scattering angle in order to calculate the ASF. This process can be avoided if the Fourier transform can be solved analytically. When this is the case, γ_s is just treated as a constant since it is not a function of the variables of integration, $\hat{x}$ and $\hat{y}$. When a numerical solution is required, multiple transforms will indeed have to be performed in order to calculate the entire ASF.

When numerical solutions of Eq. (37) are required, the parameters γ_s and γ_i have to be specified before performing the Fourier transform. Calculating the scattering distribution over the entire observation space for a given angle of incidence will therefore require a different transfer function and Fourier transform calculation for every scattering angle.

Direction cosine space is a very convenient space in which to perform the necessary calculations, as the entire observation hemisphere can be reduced to a circle with unit radius in the α, β plane. This unit circle corresponds to $\theta_s = 90°$ for all values of ϕ_s in the spherical coordinate system. It is straightforward to create a numerical grid as a two-dimensional array and then perform the calculation of the scattering function, S, given by Eq. (37), for each point in the array. For points that lie outside of the unit circle, we can simply assign a value of zero to S, since γ_s is not a real number at those locations. The calculation of the entire scattering function can thus be written as

$$S_{jk}(\alpha,\beta;\gamma_i) = K(\gamma_i)\sum_j\sum_k S(\alpha_j,\beta_k;\gamma_i,\gamma_{jk}), \tag{38}$$

where,

$$S(\alpha_j,\beta_k;\gamma_i,\gamma_{jk}) = \mathsf{F}\{G(\hat{x},\hat{y};\gamma_i,\gamma_{jk})\exp(i2\pi\beta_o\hat{y})\}|_{\alpha_s=\alpha_j,\beta_s=\beta_k}, \tag{39}$$

$$\gamma_{jk} = \sqrt{1-\alpha_j^2-\beta_k^2}, \tag{40}$$

and $K(\gamma_i)$ is the renormalization constant given by Eq. (23).

The process described above is very computationally intensive, since, for each scattering angle, we have to perform a two-dimensional discrete Fourier transform of the surface transfer function. This yields a numerical array referred to as an intermediate ASF. From this array, we extract the one data point corresponding to that scattering angle and then repeat the process for all other desired scattering angles. If the surface roughness is isotropic, the surface transfer function will be rotationally symmetric, and the two-dimensional Fourier transform operation in Eq. (39) reduces to a Hankel transform. Since the Hankel transform operation is one dimensional, this can help to reduce the computation time significantly. The process is still the same, except that, at each step, a numerical Hankel transform is performed, yielding the radial profile of the circularly symmetric intermediate ASF [32]. Using this profile, it is a simple matter to perform a one-dimensional interpolation to obtain the one point corresponding to α_j, β_k.

Since the delta function in Eq. (36) is equal to zero except when $\beta = \beta_o$, Eq. (33) yields the percentage of the total reflected power that resides in the specularly reflected light when $\gamma_s = -\gamma_i$, and, hence, also in the scattering function (i.e., the TIS). After S is known over the entire observation hemisphere, Eq. (23) is used to renormalize the volume of the scattering function to unity and thus ensure conservation of energy.

For the rough surface scattering predictions that follow, we utilized a quasi-discrete Hankel transform algorithm based on a Fourier–Bessel series expansion [55].

D. Comparison of Performance Predictions and Experimental Validation

Using the procedure for the GHS theory outlined in Subsection 3.C, we have performed a comparison of the scattered intensity predicted by the OHS theory, the MHS theory, and the GHS theory for a wavelength of 10.6 μm at incident angles of 20°, 40°, 60°, and 70°. The surface modeled was measured by O'Donnell and Mendez to have a Gaussian ACV function of the form

$$C_s(\hat{x}, \hat{y}) = \sigma_s^2 \exp[-(r^2/\ell_c^2)], \tag{41}$$

where $\sigma_s = 2.27\,\mu$m and $\ell_c = 20.9\,\mu$m [56]. Experimental data taken from [56] for incident angles of 20° and 70° is also plotted for comparison in Fig. 6. For this wavelength, the surface can be considered moderately rough since $\sigma_s/\lambda = 0.214$. It will also produce fairly wide angle scatter since the ACV width, normalized by the wavelength, is given by $\ell_c/\lambda = 1.97$.

For an incident angle of 20°, Fig. 6(a) indicates that the GHS theory predicts a peak intensity that is about 27% higher than the OHS theory, and slightly higher than the MHS theory. Although there is no significant specular reflection (TIS ~ 1), the peak of the scattered intensity distribution lies essentially in the specular direction for all three theories. Since we do not know the absolute radiometric values, we have normalized the peak values of the experimental data to be equal to that of the GHS theory. The shape of the experimental curve is in excellent agreement with that of the GHS theory.

For the 40° angle of incidence illustrated in Fig. 6(b), the three theories still all predict that there is no significant specular reflection (TIS ≥ 0.986). The MHS and GHS theories predict almost identical peak intensities (about 100% higher than the OHS theory), and the peak of the GHS intensity is centered upon the specular direction. The intensity distribution predicted by the MHS theory is shifted to slightly smaller angles. The OHS scattered intensity distribution is considerably broader than that predicted by the other two theories.

For an incident angle of 60°, Fig. 6(c) shows that the peak intensity predicted by the MHS and GHS theories has increased another 25% to 30%, with the MHS peak being somewhat higher than that of the GHS theory. The GHS and MHS

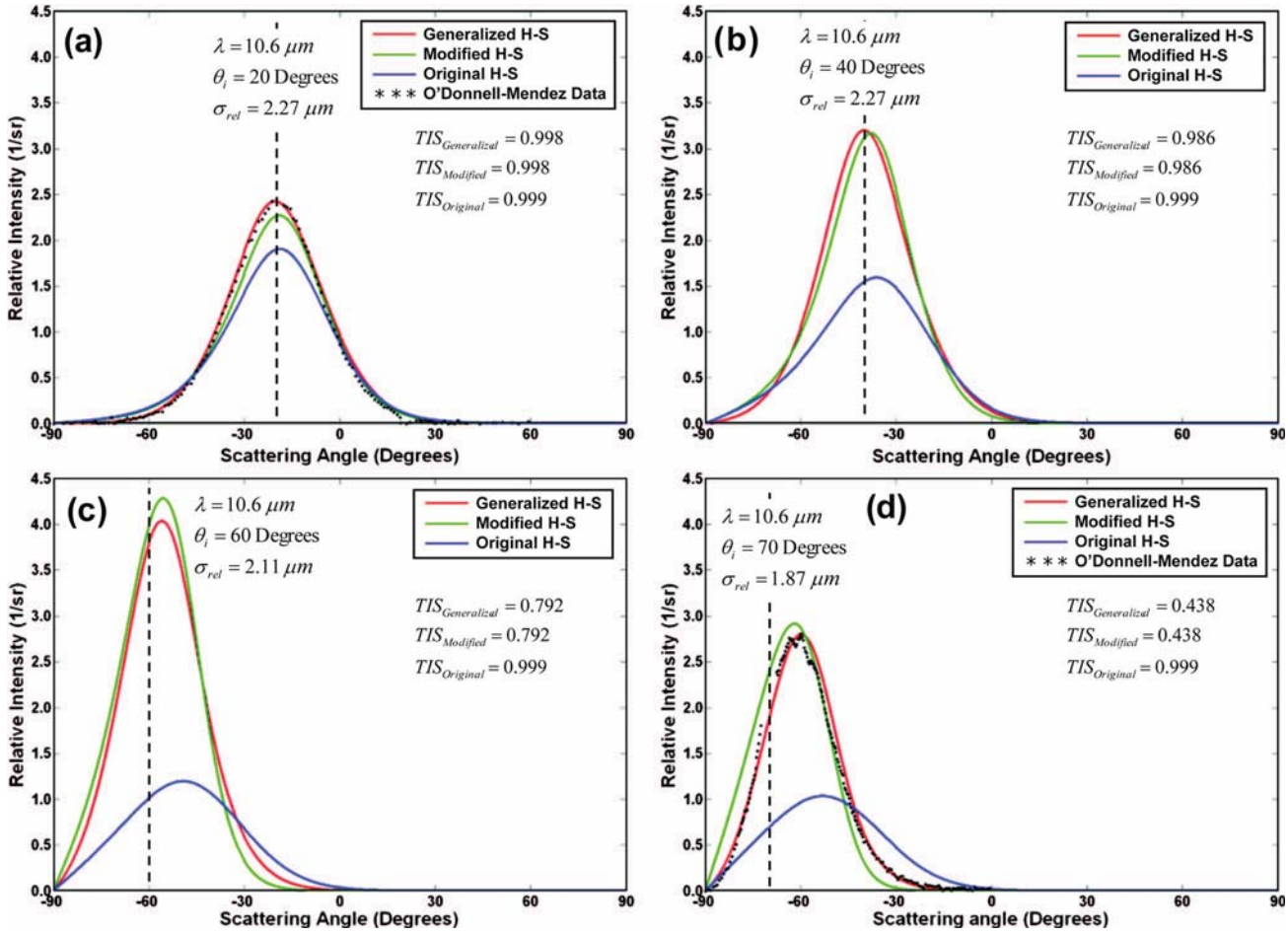

Fig. 6. (Color online) Comparison of scattered intensity predictions from the OHS, MHS, and GHS theories for different incident angles. Experimental data is also displayed for incident angles of 20° and 70°. The difference between the MHS and GHS theories is modest but significant, and the experimental data provides excellent agreement with the GHS predictions.

theories now predict a TIS equal to 0.792, which implies that ~21% of the reflected radiation is now contained in the specular beam. The OHS intensity distribution has a peak intensity about 30% as high as the other two theories, and is substantially broader.

Finally, for an angle of incidence of 70°, the peak intensities of the scattering function predicted by the GHS and MHS theories are now substantially lower, as the predicted value of the TIS has dropped to 0.438. Figure 6(d) shows a more pronounced asymmetry in the scattered intensity distribution predicted by the MHS and GHS theories. The GHS theory is an excellent fit to the experimental data, and a substantial improvement over the MHS theory. It should also be noted that experimental data is absent for those angles that represent the location of the specular beam (presumably to protect the detector), and the peak of both the measured and predicted scattered intensity distributions are shifted substantially (~10°) from the specular direction. This was one of the nonintuitive effects that the authors of [56] were unable to explain. We now understand that this shift occurs when the predicted truncated scattered radiance distribution is multiplied by the Lambert cosine function to convert it to a scattered intensity distribution.

In Fig. 7, we compare our predictions from the MHS and GHS theories with those from the experimental measurements and the classical Beckmann–Kirchhoff theory as presented by O'Donnell and Mendez for an incident angle of 70° with light of wavelength of $\lambda = 0.6328\,\mu$m. For this wavelength, the surface can be considered very rough since $\sigma_s/\lambda = 3.59$. Clearly all of the light will be diffusely scattered.

The peak of the MHS theory is shifted substantially from the peak of the GHS theory, and is also about 40% higher. The classical Beckmann–Kirchhoff theory has its peak at approximately the same angle as that of the GHS theory, and it exhibits a nonphysical discontinuity at –90°. The shapes of all three theoretical profiles are thus quite different. The agreement between the GHS theory and the experimental data is again excellent, especially considering that this is a very rough surface with a large incident angle. Figures 6 and 7 provide a convincing experimental validation of the GHS surface scatter theory for rough surfaces at large incident and scatter angles.

4. BRDF PREDICTIONS FOR ROUGH SURFACES WITH INVERSE POWER LAW PSDs

The GHS surface scatter theory described in Subsection 3.C has been shown to agree with experimental data for rough surfaces with large incident and scattered angles. We can now use the GHS surface scatter theory with confidence to calculate BRDFs for surfaces that do not satisfy the smooth-surface approximation.

Calculating BRDFs using the GHS theory does require a separate two-dimensional numerical Fourier transform to be calculated for each scattering angle of interest. It was quite computationally intense, but manageable, to make surface scatter predictions for surfaces characterized by a Gaussian PSD. Unfortunately, optical surfaces fabricated by conventional abrasive grinding and polishing techniques on ordinary amorphous glassy materials do not exhibit Gaussian PSDs. Instead, they typically exhibit an inverse power law behavior [57–59].

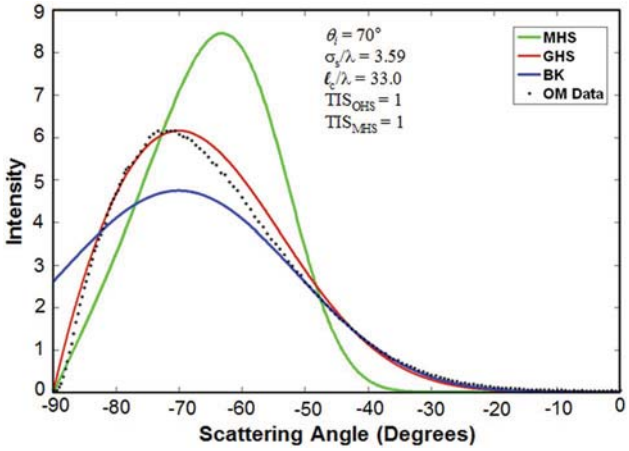

Fig. 7. (Color online) GHS predictions compared to MHS and classical Beckmann–Kirchhoff predictions. Excellent agreement is indicated between the GHS theory and the O'Donnell–Mendez experimental data for this rough surface with a large incident angle.

A. ABC or *K*-Correlation Function PSD

The *K*-correlation, or ABC, function (actually a modified Lorentzian function) has proven to be very convenient for fitting to actual metrology data from real optical surfaces [25,57–59]:

$$\mathrm{PSD}(f_x)_{1\text{-}D} = \frac{A}{[1 + (Bf_x)^2]^{C/2}}. \tag{42}$$

Assuming isotropic roughness, this one-dimensional surface PSD can be converted to the following two-dimensional surface PSD that relates more directly to the surface scatter behavior, and hence to the resulting image degradation:

$$\mathrm{PSD}(f)_{2\text{-}D} = K\frac{AB}{[1 + (Bf)^2]^{(C+1)/2}},$$
$$K = \frac{1}{2\sqrt{\pi}}\frac{\Gamma((C+1)/2)}{\Gamma(C/2)}. \tag{43}$$

There is also a convenient analytical expression for the two-dimensional Fourier transform of the above two-dimensional surface PSD. This surface ACV function is given by

$$\mathrm{ACV}(r) = (2\pi)^{1/2}\frac{A}{B}\frac{2^{-C/2}}{\Gamma(C/2)}\left(\frac{2\pi r}{B}\right)^{(C-1)/2}\mathsf{K}_{(C-1)/2}\left(\frac{2\pi r}{B}\right). \tag{44}$$

In the above expressions, A, B, and C are fitting parameters. From the hemispherical grating equation, we obtain

$$f_x = \frac{\sin\theta_s\cos\phi_s - \sin\theta_i}{\lambda}, \qquad f_y = \frac{\sin\theta_s\sin\phi_s}{\lambda}. \tag{45}$$

Also $f = \sqrt{f_x^2 + f_y^2}$, $r = \sqrt{x^2 + y^2}$, and $\mathcal{K}_{(c-1)/2}$ is the modified Bessel function of the second kind.

This inverse power law PSD does not fall to negligible values as quickly as the Gaussian PSD of the O'Donnell–Mendez surface discussed in Subsection 3.D of this paper. Hence the metrology data from typical ground and polished mirrors frequently spans 6–8 decades of dynamic range in spatial frequency. The total integral of the two-dimensional surface

PSD of Eq. (43) is equal to

$$\sigma^2_{\text{total}} = \frac{2\pi KAB}{(C-1)B^2}, \quad \text{for } C > 1.0. \tag{46}$$

For $C \le 1.0$, the integral does not converge, and the total (or intrinsic) surface roughness is infinite. However, for all values of C, the maximum relevant surface roughness is finite because roughness with a spatial frequency greater than that which would diffract, or scatter, light into an angle greater than 90° from the surface normal produces only evanescent waves, which do not result in additional scattered light losses.

B. Implementation of the FFTLog Hankel Transform Algorithm

Performing the required Fourier transforms numerically using traditional fast Fourier transform (FFT) algorithms becomes very computationally intensive (prohibitively so for surface PSDs requiring a large dynamic range in spatial frequency). In addition, the quasi-discrete Hankel transform algorithm discussed in Subsection 3.C does not seem to work well with the K-correlation functions described above. We therefore utilized an implementation of the FFTLog algorithm [60] to calculate BRDFs from surface metrology data expressed in the form of an inverse power law surface PSD.

The FFTLog algorithm is used to compute the fast Fourier or Hankel (i.e., Fourier–Bessel) transform of a periodic sequence of logarithmically spaced data points. It is particularly useful for applications where the power spectrum extends over many orders of magnitude in spatial frequency, f, and varies smoothly in $\log f$. It has been numerically validated to be accurate over a very impressive 25 decades of dynamic range in spatial frequency when Fourier transforming a well-behaved ABC function [61].

C. BRDF Predictions from Actual Optical Surface Metrology Data

Figure 8 illustrates a surface PSD constructed from metrology data from an actual state-of-the-art extreme-UV (EUV) telescope mirror. Note that each metrology instrument is inherently band limited; hence, the surface PSD, over the entire range of relevant spatial frequencies, was pieced together from the results of measurements from separate metrology instruments. An ABC function of the form described by Eq. (43) was then fit to the metrology data.

The ABC function fit to the metrology data was then Fourier transformed using the analytic expression given by Eq. (44). The resulting ACV function was substituted into Eq. (29) for the surface transfer function of the GHS surface scatter theory described in Subsection 3.C. This two-parameter family of surface transfer functions was then numerically Fourier transformed multiple times (using the FFTLog algorithm discussed in Subsection 4.B) according to Eq. (30) to obtain the BRDF profiles illustrated in Fig. 9 [61].

In accordance with the nonparaxial scalar diffraction theory [19–21] upon which the GHS surface scatter theory is based, each BRDF profile was renormalized (by varying the parameter A) such that the integral of the scattered intensity over a complete hemisphere equals the value of TIS predicted by Eq. (34) when $\theta_s = -\theta_i$. Figure 9 shows BRDF profiles calculated for eight different wavelengths ranging from 1000 Å (vacuum UV) to 93.9 Å (EUV). The values of the ABC parameters characterizing the mirror surface are indicated on the figure. Note that the TIS, as calculated by Eq. (34), varies from less than 1% for $\lambda = 1000$ Å to over 56% for $\lambda = 93.9$ Å.

In Fig. 10, the same BRDF profiles are plotted as a function of $\beta = \sin\theta_s$ on a log–log scale. They appear to have the same shape as the surface PSD, as expected for the long wavelengths that satisfy the smooth-surface approximation of the classical Rayleigh–Rice expression [25]:

$$\text{BRDF}(\theta_s) = \frac{16\pi^2}{\lambda^4}\cos\theta_i \cos\theta_s Q\text{PSD}(f), \qquad f = \sin\theta_s/\lambda. \tag{47}$$

The Rayleigh–Rice surface scatter theory is a rigorous vector perturbation theory; hence Q is the polarization reflectance that is discussed thoroughly by Stover [25]. The relevant roughness is only implicit in the PSD of Eq. (47). The TIS historically associated with the Rayleigh–Rice theory is given by [25]

$$\text{TIS}_{RR} = (4\pi\cos\theta_i\sigma_s/\lambda)^2. \tag{48}$$

However, today it would be agreed that the σ_s should be replaced by the relevant roughness, σ_{rel}.

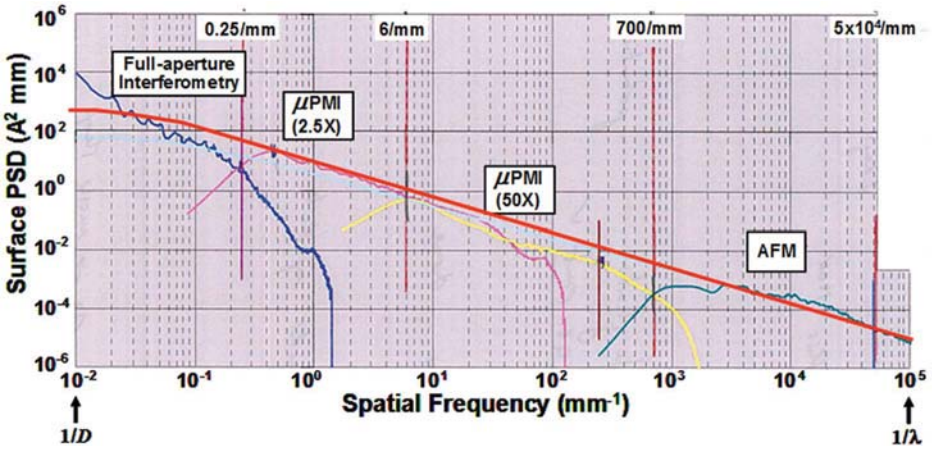

Fig. 8. (Color online) Composite surface PSD function determined from four different metrology instruments. An ABC, or K-correlation, function has been fit to the experimental data to characterize the surface over the entire range of relevant spatial frequencies.

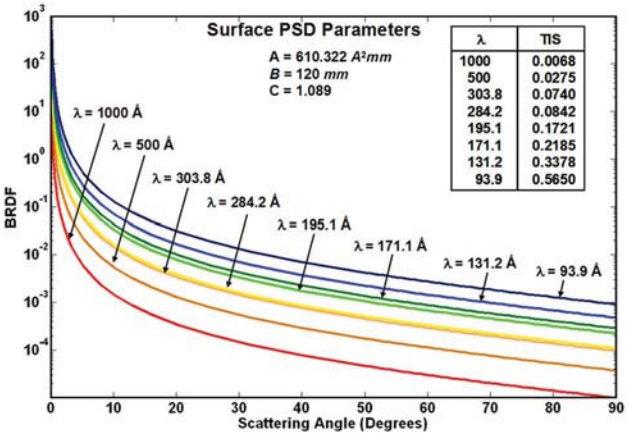

Fig. 9. (Color online) These BRDF profiles were numerically calculated from the real metrology data (surface PSD) illustrated in Fig. 8. The GHS surface scatter theory was used for this moderately rough surface. The FFTLog algorithm was implemented in the calculations.

Note that, in Fig. 10, the scattered radiance increases and the position of the shoulder shifts to the left with decreasing wavelength. The slope of the inverse power law behavior does not appear to change significantly with wavelength. However, this slope does begin to change significantly as $\sigma_{\mathrm{rel}}/\lambda$ becomes larger.

In Fig. 11 we compare the BRDF profile for $\lambda = 93.9\,\text{Å}$ as predicted by the GHS and the Rayleigh–Rice surface scatter theories [61]. Although the difference appears small on this log–log plot covering almost 20 decades on the vertical axis, the expanded inset shows that the peak of the BRDF function predicted by the Rayleigh–Rice theory is more than a factor of 2 higher than that predicted by the GHS theory. The corresponding percent error in the peak value of the BRDF predicted by the Rayleigh–Rice theory for the other wavelengths is also tabulated in Fig. 10. This percent error decreases monotonically with increasing wavelength, reducing to less than 0.3% error for a wavelength of 1000 Å. Again, this is to be expected as $\sigma_{\mathrm{rel}}/\lambda = 0.00657$ for $\lambda = 1000\,\text{Å}$, and this is well within the smooth-surface approximation of the Rayleigh–Rice vector perturbation theory.

There is a second inset in Fig. 11 that shows an expanded view of the two curves as they approach a scattering angle of 90°. The BRDF predicted by the Rayleigh–Rice theory dives to zero as it approaches 90°, whereas the BRDF predicted by the GHS theory makes a modest dip but remains distinctly finite. This behavior is caused by the different obliquity factors of the two theories, and will be discussed in detail in Section 5. This forcing of the BRDF to zero at 90° by the Rayleigh–Rice obliquity factor is perhaps the cause of the ubiquitous "hook" in surface PSDs predicted by surface scatter measurements [62,63].

5. SMOOTH-SURFACE APPROXIMATION TO THE GHS SURFACE SCATTER THEORY

When the roughness of the surface is small compared to the wavelength of the incident light ($\hat{\sigma}_{\mathrm{rel}} \ll 1$), the surface transfer function is still given by Eq. (29); however, we can make the following explicit approximations to its constituent parts expressed in Eq. (32)–(34):

$$A(\gamma_i, \gamma_s) \approx 1 - [2\pi\hat{\sigma}_{\mathrm{rel}}(\gamma_i + \gamma_s)]^2, \tag{49}$$

$$B(\gamma_i, \gamma_s) \approx [2\pi\hat{\sigma}_{\mathrm{rel}}(\gamma_i + \gamma_s)]^2, \tag{50}$$

$$G(\hat{x}, \hat{y}) \approx C_s(\hat{x}, \hat{y})/\sigma_s^2. \tag{51}$$

The scattering function is still given by Eq. (39), and the BRDF by Eq. (13); hence

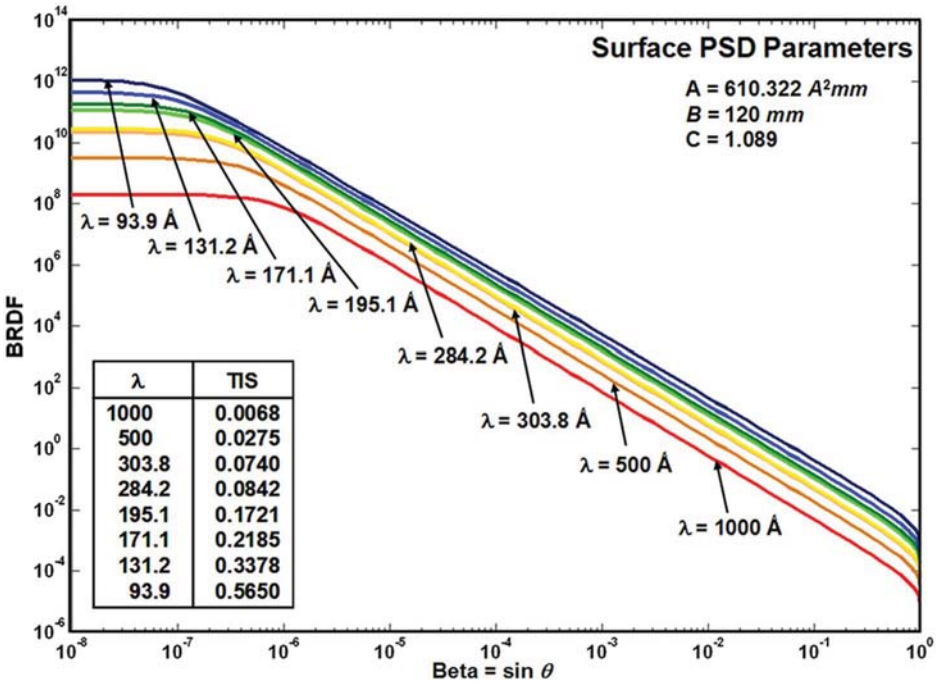

Fig. 10. (Color online) The BRDF profiles illustrated in Fig. 9 are plotted here on a log–log scale as a function of $\beta = \sin(\theta)$. They now exhibit the shape of the surface PSD as expected from the Rayleigh–Rice theory for the long wavelengths.

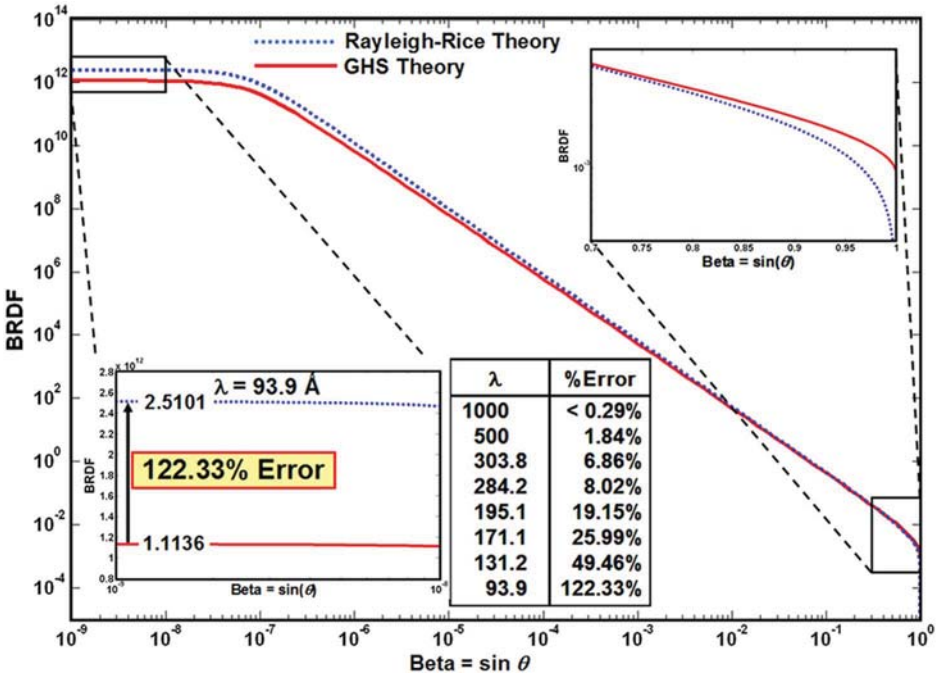

Fig. 11. (Color online) Comparison of the BRDF profile predicted by the GHS and Rayleigh–Rice surface scatter theories shows that, for $\lambda = 93.9$ A, the Rayleigh–Rice theory results in a peak BRDF value 122% higher than the GHS theory (lower left inset). Errors for other wavelengths are tabulated. Upper right inset shows distinctly finite value of the GHS curve at a 90° scattering angle.

$$\mathrm{BRDF} = \frac{4\pi^2}{\lambda^4} K(\cos\theta_i + \cos\theta_s)^2 Q \frac{\sigma_{\mathrm{rel}}^2}{\sigma_s^2} \mathrm{PSD}(f_x, f_y). \quad (52)$$

Here the $\mathrm{PSD}(f_x, f_y)$ is the two-sided, two-dimensional surface PSD function and f_x and f_y are given by Eq. (45). Note that we have quasi-vectorized our scalar scattering theory by merely substituting the polarization reflectance, Q, from the Rayleigh–Rice theory for the scalar reflectance R.

A. Comparison with the Rayleigh–Rice Theory

Before proceeding to compare the predictions of the smooth-surface approximation of the GHS theory with the classical Rayleigh–Rice theory, we briefly review the definitions of a few radiometric quantities [64]. This will aid in the following discussion of the effects of different obliquity factors in the two theories:

$$\mathrm{Irradiance} = E = \frac{dP}{dA} \quad (\text{radiant power/area}),$$

$$\mathrm{Radiant\ Intensity} = I = \frac{dP}{d\omega} \quad (\text{radiant power/steradian}),$$

$$\mathrm{Radiance} = L = \frac{d^2P}{d\omega dA\cos\theta} \quad (\text{radiant power /steradian projected area}). \quad (53)$$

In the past, scientists have generally used the word intensity to mean the flow of energy per unit area per unit time. However, by international, if not universal, agreement, that term is slowly being replaced by the word irradiance [65]. Furthermore, the definition of intensity provided by Eq. (53) is one of seven SI base quantities (including length, mass, time, etc.) from which all other physical quantities are derived [66].

The BRDF, previously defined in Eq. (11) as the reflected radiance divided by the incident irradiance, is a computed quantity calculated by dividing the measured radiant intensity by the cosine of the scattered angle. Angle-resolved scatter (ARS) is a term used by some segments of the radiometric community for this measured scattered intensity [67]. The differential scattered intensity predicted from the classical Rayleigh–Rice vector perturbation theory is given by [1,25]

$$\mathrm{ARS}(\theta_s, \phi_s)d\omega_s = \frac{1}{P_i}\left(\frac{dP}{d\omega}\right)_s d\omega_s = \frac{16\pi^2}{\lambda^4}\cos\theta_i \cos^2\theta_s Q \mathrm{PSD}(f_x, f_y)d\omega_s, \quad (54)$$

where $d\omega_s = \sin\theta_s d\theta_s d\phi_s$ is the differential solid angle subtended by the small collecting aperture of the instrument scanned over the observation hemisphere when making the ARS measurements.

Recalling that radiant intensity is obtained by multiplying radiance by Lambert's cosine function ($\cos\theta_s$) [64], the corresponding quantity predicted by the smooth-surface approximation to the GHS surface scatter theory is obtained from Eq. (52):

$$\mathrm{ARS}(\theta_s, \phi_s)d\omega_s = \frac{1}{P_s}\left(\frac{dP}{d\omega}\right)_s d\omega_s = \frac{4\pi^2}{\lambda^4} K(\cos\theta_i + \cos\theta_s)^2 \times \cos\theta_s Q \frac{\sigma_{\mathrm{rel}}^2}{\sigma_s^2} \mathrm{PSD}(f_x, f_y)d\omega_s, \quad (55)$$

Figure 12 shows a direct comparison of scattered intensity profiles predicted by the classical Rayleigh–Rice theory, the smooth-surface approximation to the GHS theory, and the GHS theory for a perfectly conducting, smooth surface characterized by a Gaussian ACV function as described in Eq. (41). In Fig. 12(a), we have normal incidence and a normalized ACV

width (ℓ_c/λ) large enough that a vanishingly small portion of the surface PSD extends beyond a spatial frequency of $1/\lambda$. In Fig. 12(b), we have a 60° incident angle, but have increased the ACV width such that the width of the surface PSD is reduced to the point that, once again, only an infinitesimal portion of its volume lies outside of the displaced circle of radius $1/\lambda$ illustrated in Fig. 3(a). Thus, for both cases, $\sigma_{\text{rel}} \cong \sigma_s$. Under these conditions, all three theories result in virtually identical predictions.

However; even for smooth surfaces, as the ACV width decreases and the surface PSD broadens such that σ_{rel} becomes less than σ_s, the Rayleigh–Rice predictions increasingly disagree with the GHS predictions as illustrated in Fig. 13. The smooth-surface approximation to the GHS theory continues to agree with the GHS theory for smooth surfaces even when $\sigma_{\text{rel}} < \sigma_s$ because of the σ_{rel} rather than σ_s in Eq. (50) and the renormalization constant, K, in Eq. (52).

For moderately rough surfaces where the ACV width is large enough such that $\sigma_{\text{rel}} \cong \sigma_s$, the Rayleigh–Rice theory and the $\text{GHS}_{\text{Smooth}}$ theory agree, as shown in Fig. 14, but are both inaccurate due to their explicit smooth-surface approximations. Having been shown to agree with the Rayleigh–Rice theory for smooth surfaces when $\sigma_{\text{rel}} \cong \sigma_s$, and with experimental measurements for very rough surfaces and large incident angles (Fig. 6), the GHS theory is presumed to be accurate.

Finally, we show two cases for moderately rough surfaces and $\sigma_{\text{rel}} < \sigma_s$. In Fig. 15(a), both the Rayleigh–Rice and the $\text{GHS}_{\text{Smooth}}$ curves are too high because of their explicit smooth-surface approximation. As in Fig. 13(a), the $\text{GHS}_{\text{Smooth}}$ curve is higher than the Rayleigh–Rice curve because of the renormalization that is performed. In Fig. 15(b), the Rayleigh–Rice and the $\text{GHS}_{\text{Smooth}}$ again exhibit scattered intensity curves that are considerably higher than that of the GHS theory. The Rayleigh–Rice curve is now higher than that of the $\text{GHS}_{\text{Smooth}}$ theory because σ_s is substantially larger than σ_{rel}.

Figures 12–15 illustrate scattered intensity, or ARS predictions, rather than BRDF curves. The extra $\cos\theta_s$ that appears in the obliquity function for scattered intensity in Eqs. (54) and (55) obscures some substantial differences that become apparent when we compare BRDF profiles predicted by the different theories.

Figure 16 shows a direct comparison of the BRDF predictions by the classical Rayleigh–Rice theory given by Eq. (47) and the smooth-surface approximation to the GHS theory given by Eq. (52) for both a Gaussian PSD and a K-correlation (inverse power law) PSD. The only difference between the two theories are the slightly different obliquity factors, the renormalization constant, K, and the ratio $\sigma_{\text{rel}}^2/\sigma_s^2$ in Eq. (52) for the GHS theory. The renormalization constant assures that the integral of the GHS scattering function will always be equal to the TIS as predicted by the quantity B in Eq. (50) when $\theta_s = -\theta_i$.

Note that the obliquity factors are approximately equal for small incident and scattering angles. In fact, they are exactly equal when $\theta_s = \pm\theta_i$. The striking difference in the BRDF profiles illustrated in Fig. 16 is that the Rayleigh–Rice theory drives the BRDF to zero at ±90°, regardless of the nature of the surface PSD, whereas the GHS theory does not.

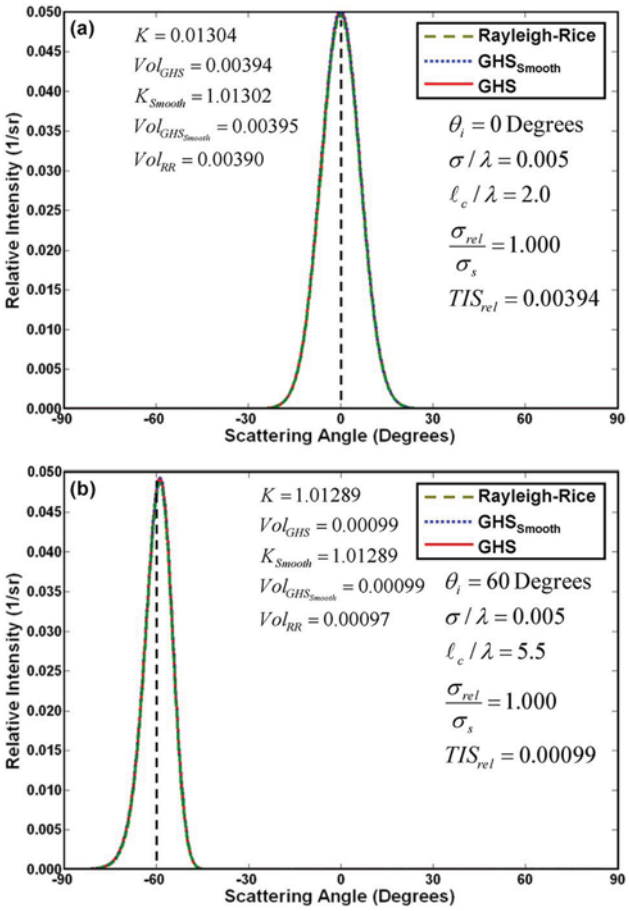

Fig. 12. (Color online) The GHS surface scatter theory and its smooth-surface approximation are numerically validated by the well-known Rayleigh–Rice surface scatter theory for smooth surfaces and $\sigma_{\text{rel}} \cong \sigma_s$.

B. Inverse Scattering Problem

Equations (47) and (52) can be rewritten to allow the calculation of surface characteristics from BRDF measurements (the inverse scattering problem):

$$\text{PSD}(f_x,f_y) = \frac{\lambda^4}{4\pi^2}\frac{\sigma_s^2}{\sigma_{\text{rel}}^2}\frac{\text{BRDF}}{K(\cos\theta_i + \cos\theta_s)^2 Q}, \tag{56}$$

$$\text{PSD}(f_x,f_y) = \frac{\lambda^4}{16\pi^2}\frac{\text{BRDF}}{\cos\theta_i \cos\theta_s Q}. \tag{57}$$

The Rayleigh–Rice surface scatter theory is widely accepted for smooth surfaces and has been extensively used for decades for large scattered and incident angles. However, when used to predict surface PSDs from BRDF measurements, the Rayleigh–Rice theory yields a ubiquitous and annoying "hook" at the high-spatial-frequency end of the predicted PSDs [62,63]. These hooks in the predicted PSD are generally ignored because it is assumed that they are not real since their location on the predicted PSD shifts with incident angle.

The questionable behavior of BRDFs diving to zero at $\theta_s = \pm 90°$, regardless of the nature of the surface PSD, suggests that the puzzling and ubiquitous hook might be a

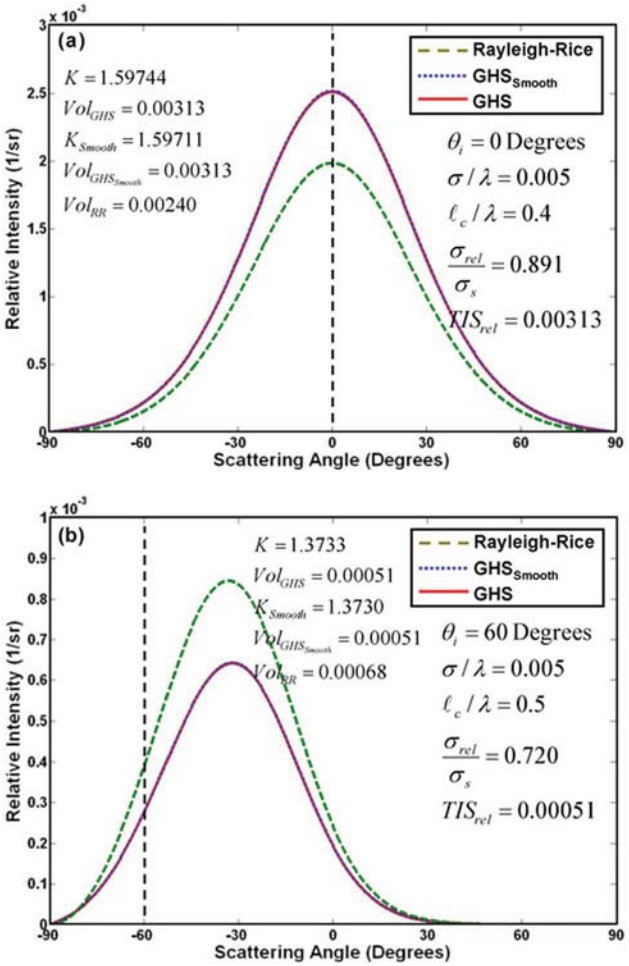

Fig. 13. (Color online) Even for smooth surfaces, the well-known Rayleigh–Rice theory increasingly disagrees with the GHS theory as the ACV width decreases and σ_{rel} becomes smaller than σ_s. The $\mathrm{GHS}_{\mathrm{Smooth}}$ theory continues to agree with the GHS theory as long as the surface is smooth.

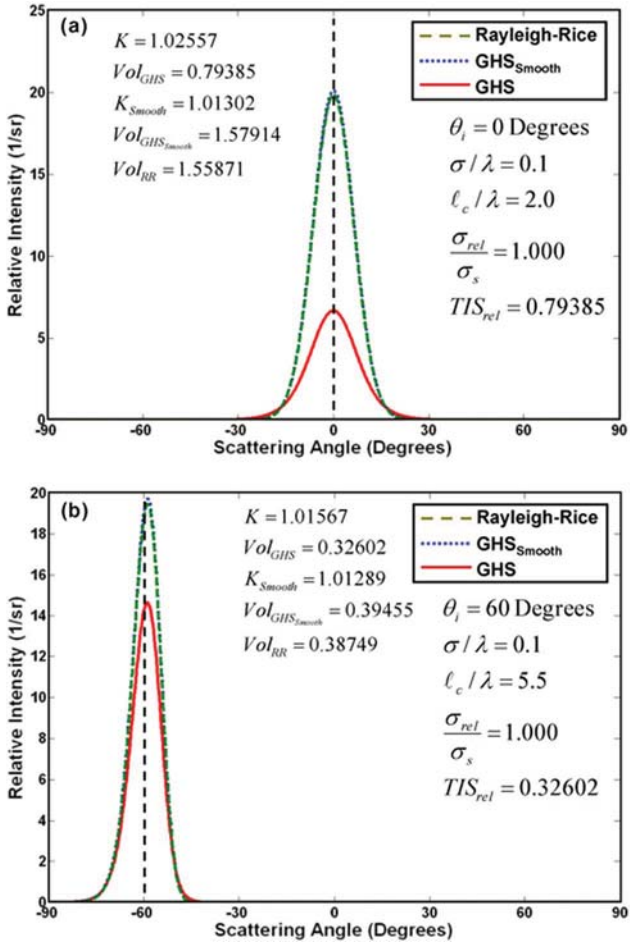

Fig. 14. (Color online) For moderately rough surfaces where the ACV width is large enough such that $\sigma_{\mathrm{rel}} \cong \sigma_s$, the Rayleigh–Rice theory and the $\mathrm{GHS}_{\mathrm{Smooth}}$ theory agree but are both inaccurate due to their explicit smooth-surface approximations. The GHS theory is presumed to be accurate.

computational artifact of an incorrect obliquity factor in the Rayleigh–Rice theory. In an attempt to resolve this dilemma, Stover [62] made extensive BRDF measurements on several smooth surfaces. He carefully measured and recorded scattered intensity data at closely spaced angular intervals over the entire range of scattered angles, all the way out to 89.6°. Figure 17 shows the meticulous scattered intensity measurements from a clean, smooth, gold-coated surface from which the BRDF was calculated by merely dividing by the cosine of the scattered angle.

The measured radiant intensity (watts/steradian) was divided by the incident radiant power resulting in the indicated units of inverse steradians. Note that the directly measured radiant intensity data turns toward zero as the scattered angle approaches 90° (as it must). However, the BRDF curve does not show signs of diving toward zero for large scatter angles, as predicted by the Rayleigh–Rice theory.

Figure 18 shows the surface PSD as predicted by both the Rayleigh–Rice surface scatter theory and the smooth-surface approximation of the GHS surface scatter theory ($K \cong \sigma_s/\sigma_{\mathrm{rel}} \cong 1$). Reference [62] should be studied to appreciate the care that was taken to assure that measurement errors or instrumental effects were not the cause of the huge hook in the surface PSD predicted by the Rayleigh–Rice theory. Note that there is virtually no evidence of a hook in the PSD predicted from the smooth-surface approximation of the GHS surface scatter theory from the BRDF data illustrated in Fig. 7.

Although we originally thought that we had discovered this new obliquity factor that seems to eliminate the undesirable computational artifacts in the surface PSDs predicted from BRDF measurements, it is interesting to note that, in his 1989 SPIE Proceedings paper [68], Church performed a Fresnel–Kirchhoff derivation of surface scatter and obtained an obliquity factor identical to that in Eq. (56). However, he considered this scalar treatment to be an approximation to the more rigorous Rayleigh–Rice vector perturbation theory and, to our knowledge, never performed a comparison of the effects of the two obliquity factors upon the calculation of the surface PSD from BRDF data.

Other researchers have also recently (and independently) verified that the GHS obliquity factor eliminates the hook at the high-spatial-frequency end of surface PSDs predicted from ARS measurements [69]. However, some researchers have other explanations for this behavior, resulting in ongoing discussions.

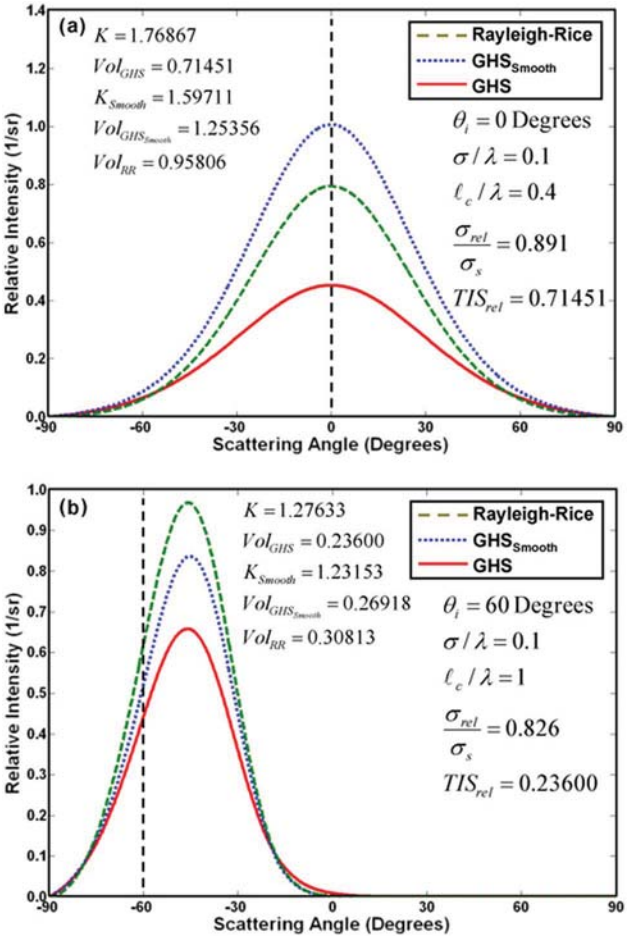

Fig. 15. (Color online) For moderately rough surfaces where $\sigma_{rel} < \sigma_s$, the Rayleigh–Rice and the GHS_{Smooth} theory both produce predictions for the scattered intensity that are too high, with the worst offender depending upon the specific value of the renormalization constant and the ratio σ_{rel}/σ_s.

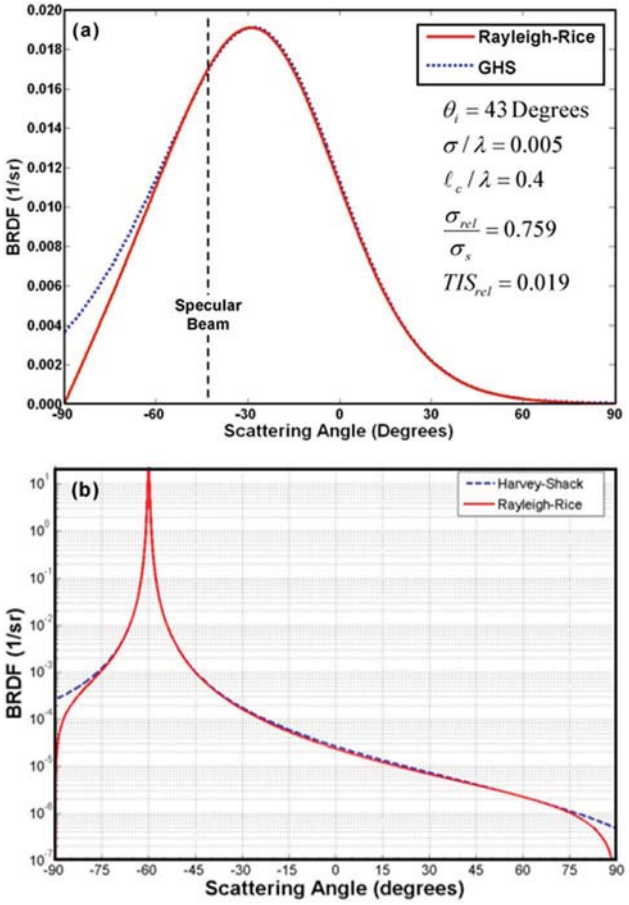

Fig. 16. (Color online) Comparison of BRDF predictions from the Rayleigh–Rice theory and the smooth-surface approximation to the GHS surface scatter theories for smooth surfaces with (a) a Gaussian PSD and (b) a K-correlation (inverse power law) PSD. Note the difference in the two predictions for $\theta_s \approx 90$ degrees.

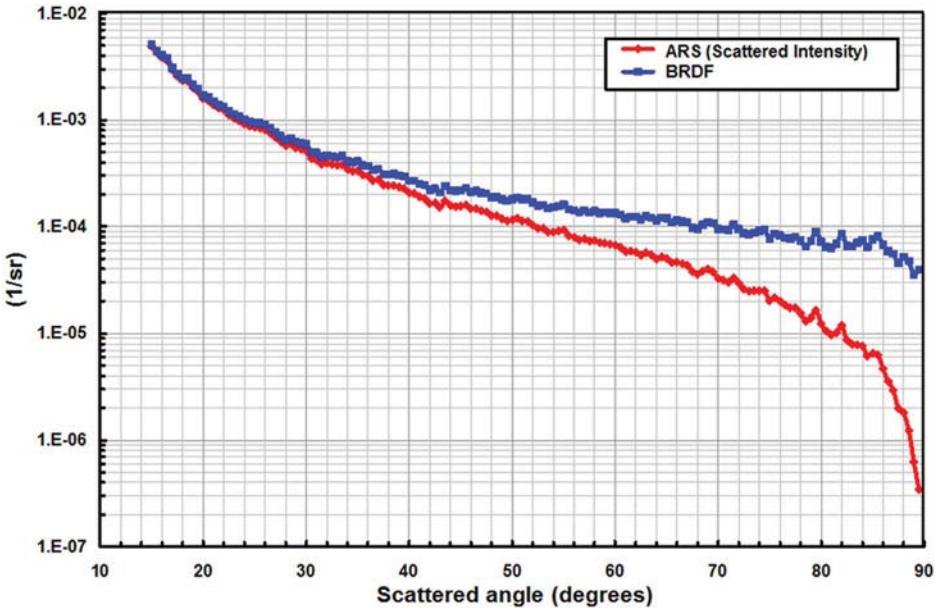

Fig. 17. (Color online) Meticulously measured, high-angular-resolution, relative intensity measurements, and the corresponding BRDF profile, extending to a scatter angle of 89.6°.

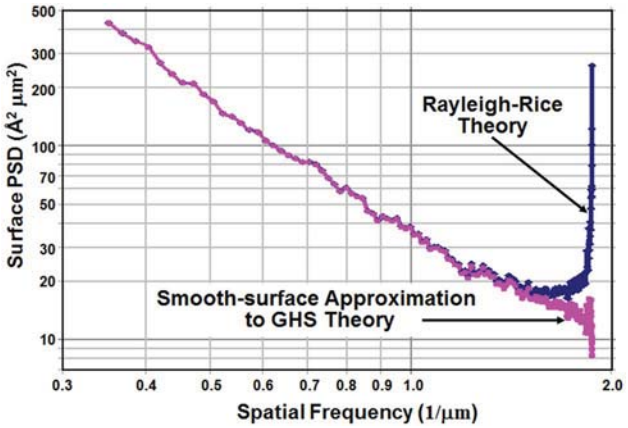

Fig. 18. (Color online) Illustration of the very prominent "hook" in the surface PSD predicted by the Rayleigh–Rice theory, and the virtual absence of any such hook predicted by the smooth-surface approximation to the GHS surface scatter theory.

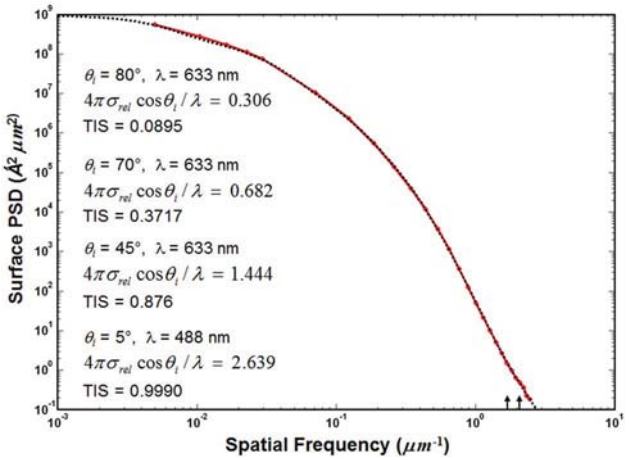

Fig. 20. (Color online) Surface PSD calculated from Eq. (57) illustrated along with a fitting function to be used as input for the GHS surface scatter theory to calculate BRDFs at different wavelengths and incident angles.

6. PREDICTING BRDFS FOR ARBITRARY WAVELENGTHS AND INCIDENT ANGLES

Although the difference in the obliquity factors of the two smooth-surface scattering theories is interesting, it does not significantly affect the TIS for moderately rough surfaces. Of more practical importance is the fact that the GHS surface scatter theory finally makes it possible to predict BRDFs for arbitrary wavelengths and incident angles for a moderately rough surface from measured BRDF data at a single wavelength and incident angle.

It is generally accepted that the inverse scattering problem of predicting the surface PSD from BRDF measurements is only possible for smooth surfaces [25]. However, the actual requirement is that the rms phase variation of the reflected wavefront is small [3]:

$$4\pi\sigma_{\mathrm{rel}}\cos\theta_i/\lambda \ll 1. \tag{58}$$

Clearly, for a moderately rough surface ($\sigma_{\mathrm{rel}} \sim \lambda$), a large incident angle ($\theta_i \sim 80°$) can be chosen such that the above condition is still satisfied.

Figure 19 illustrates BRDF data measured at different wavelengths and incident angles from a moderately rough, clean silicon surface [62]. The irregularities in the left side of the BRDF profiles are caused by the detector mechanism blocking the incident beam, and that same mechanism producing glints as it enters and emerges from the incident beam. Using the measured BRDF data for $\lambda = 633\,\mathrm{nm}$ and $\theta_i = 80°$, the smooth-surface criterion of Eq. (58) is marginally satisfied with a value of 0.306. We can thus use Eq. (56) to perform the inverse scattering calculation with the smooth-surface approximation to the GHS surface scatter theory to obtain an estimate of the surface PSD (assume that $K \cong \sigma_s/\sigma_{\mathrm{rel}} \cong 1$).

Figure 20 shows the resulting surface PSD that has been fit with the sum of five ABC functions. Note the arrows on the abscissa that indicate the maximum relevant spatial frequency

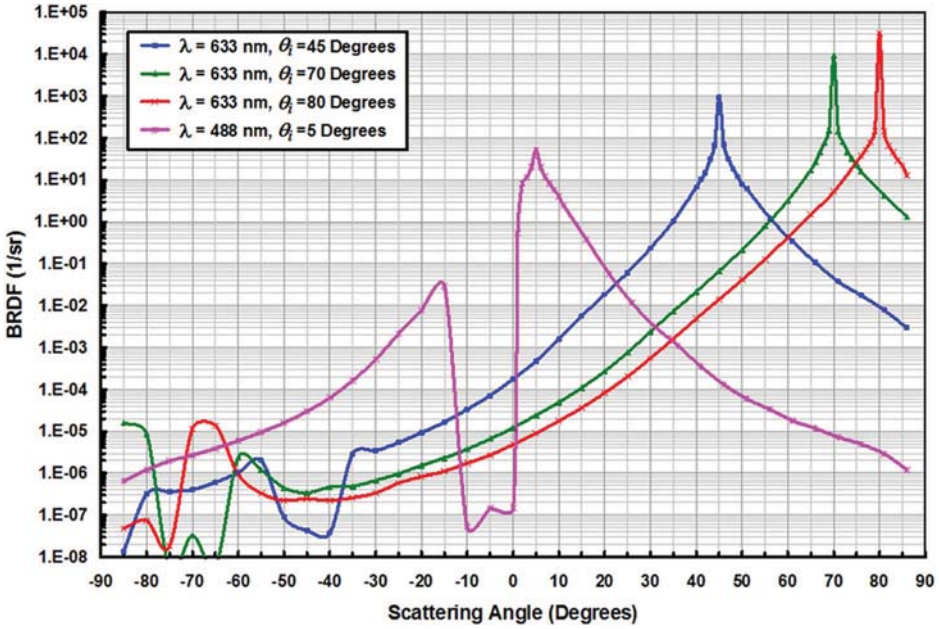

Fig. 19. (Color online) BRDF scans were taken from the back side of a clean silicon wafer for incident angles of 5°, 45°. 70°, and 80°. A shorter wavelength of 488 nm was used at $\theta_i = 5°$ to increase the apparent "roughness" as expressed by Eq. (58).

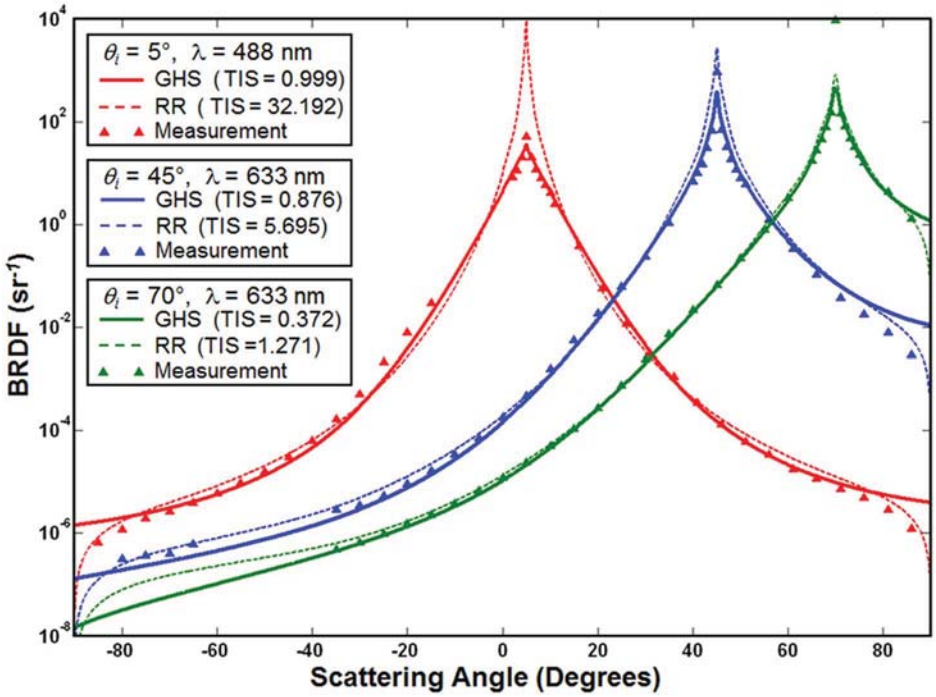

Fig. 21. (Color online) BRDFs predicted with both the GHS and the Rayleigh–Rice surface scatter theories are compared to experimental measurements for three cases that do not satisfy the smooth-surface criterion.

for the wavelengths of 633 and 488 nm (at normal incidence). We have also evaluated the roughness criterion of Eq. (58) and the resulting TIS for the four cases of interest and tabulated the values on Fig. 20, along with the calculated surface PSD curve.

We can now use this predicted surface PSD as input to the GHS surface scatter theory to calculate the BRDF at other wavelengths and incident angles that clearly do not satisfy the smooth-surface approximation. Figure 21 shows excellent agreement between the theoretical predictions with the GHS theory and the corresponding experimental BRDF measurements for a wavelength of 633 nm and incident angles of 70° and 45°, and for a wavelength of 488 nm and an incident angle of 5°.

Also indicated in Fig. 21 are similar predictions of the BRDF made by applying the Rayleigh–Rice surface scatter theory. In these cases, the PSD used was also calculated with the Rayleigh–Rice theory. The smooth-surface approximation inherent to the Rayleigh–Rice theory results in substantial overestimating of the BRDF at small to moderate angles (by more than 2 orders of magnitude for the smallest incident angle of 5°). Although the Rayleigh–Rice predictions are quite good at very large scattering angles, the integral of the resulting BRDF over the full hemisphere results in unrealistically large values for the TIS, exceeding the physical limit of TIS = 1.0 for incident angles of 5° and 45°.

7. SUMMARY AND CONCLUSIONS

Rayleigh–Rice [1,2] or classical Beckmann–Kirchhoff [3] theories are commonly used to predict surface scatter behavior. The Rayleigh–Rice vector perturbation theory agrees well with experimental wide-angle scatter measurements from smooth ($4\pi\sigma_{\mathrm{rel}}\cos\theta_i/\lambda \ll 1$) surfaces for large incident and scattering angles. The classical Beckmann–Kirchhoff scattering theory is valid for rougher surfaces, but contains a paraxial (small-angle) assumption that limits its ability to accurately handle wide-angle scattering and large angles of incidence. The closed-form equations provided by Beckmann are also limited to scattering surfaces with Gaussian ACV functions [3]. A recently developed nonparaxial scalar diffraction theory [19–21] has led to the development of a generalized linear systems formulation of surface scatter theory that appears to suffer from neither of the fundamental limitations of the classical Rayleigh–Rice and Beckmann–Kirchhoff theories.

The derivation of a two-parameter family of surface transfer functions that characterizes general surface scatter phenomena results in a rather computationally intensive process for obtaining two-dimensional scattered light behavior. However, for isotropic roughness, the computational time is greatly reduced. Extensive parametric performance predictions indicate excellent agreement with experimental data for rough surfaces, even for large incident and scattered angles. This GHS surface scatter theory also exhibits excellent agreement with the well-established Rayleigh–Rice vector perturbation surface scatter theory (for TE, or *s* polarization) for smooth surfaces and large correlation widths (comparisons performed for surfaces with Gaussian ACV functions).

Until very recently, BRDF predictions for rough surfaces with inverse power law PSDs have been problematic due to the large dynamic range of relevant spatial frequencies. This problem has been solved by the implementation of a numerical FFTLog algorithm that uses logarithmically spaced samples.

Furthermore, a smooth-surface approximation of the GHS surface scatter theory has provided a somewhat modified obliquity factor from that of the classical Rayleigh–Rice theory. This modified obliquity factor appears to eliminate the troublesome and annoying hook in surface PSDs predicted from BRDF measurements that has plagued stray light analysts for decades.

Finally, we have shown the GHS surface scatter theory to be a useful tool for addressing the inverse scattering problem. It can be used to predict surface PSDs for moderately rough surfaces if the BRDF data was measured at sufficiently large angles to satisfy the smooth-surface criterion stated by Eq. (58). This surface PSD can then be used to make BRDF predictions with the GHS surface scatter theory at arbitrary wavelengths and incident angles.

REFERENCES AND NOTES

1. S. O. Rice, "Reflection of electromagnetic waves from slightly rough surfaces," Commun. Pure Appl. Math. **4**, 351–378 (1951).
2. E. L. Church, H. A. Jenkinson, and J. M. Zavada, "Relationship between surface scattering and microtopographic features," Opt. Eng. **18**, 125–136 (1979).
3. P. Beckmann and A. Spizzichino, *The Scattering of Electromagnetic Waves from Rough Surfaces* (Pergamon, 1963).
4. J. E. Harvey, "Light-scattering characteristics of optical surfaces," Ph.D. dissertation (University of Arizona, 1976).
5. J. E. Harvey, "Surface scatter phenomena: a linear, shift-invariant process," Proc. SPIE **1165**, 87–99 (1989).
6. C. L. Vernold and J. E. Harvey, "A modified Beckmann-Kirchhoff scattering theory," Proc. SPIE **3426**, 51–56 (1998).
7. J. E. Harvey, A. Krywonos, and C. L. Vernold, "Modified Beckmann-Kirchhoff scattering model for rough surfaces with large incident and scattered angles," Opt. Eng. **46**, 078002 (2007). One of the ten most frequently downloaded SPIE papers and articles (from SPIE Digital Library) in August 2007.
8. H. Ragheb and E. Hancock, "The modified Beckmann-Kirchhoff scattering theory for rough surface analysis," Pattern Recog. **40**, 2004–2020 (2007).
9. Y. Sun, "Statistical ray method for deriving reflection models of rough surfaces," J. Opt. Soc. Am. A **24**, 724–744 (2007).
10. H. Ragheb and E. R. Hancock, "Testing new variants of the Beckmann-Kirchhoff model against radiance data," Comput. Vis. Image Understanding **102**, 145–168 (2006).
11. A. Robles-Kelly and E. R. Hancock, "Estimating the surface radiance function from single images," Graph. Models **67**, 518–548 (2005).
12. H. Ragheb and E. R. Hancock, "Surface radiance correction for shape from shading," Pattern Recog. **38**, 1574–1595 (2005).
13. H. Ragheb and E. R. Hancock, "Adding subsurface attenuation to the Beckmann-Kirchhoff theory," in *Pattern Recognition and Image Analysis*, Part 2, Vol. 3523 of Lecture Notes in Computer Science (Springer-Verlag, 2005), pp. 247–254.
14. A. Robles-Kelly and E. R. Hancock, "Radiance function estimation for object classification," in *Progress in Pattern Recognition, Image Analysis and Applications*, Vol. 3287 of Lecture Notes in Computer Science (Springer-Verlag, 2004), pp. 67–75.
15. P. Hermansson, G. Forssell, and J. Fagerstrom, "A review of models for scattering from rough Surfaces," Scientific Report FOI-R-0988-SE (Swedish Defense Research Agency, Nov. 2003).
16. H. Ragheb and E. R. Hancock, "Rough surface correction and re-illumination using the modified Beckmann model," in *Computer Analysis of Images and Patterns: 10th International Conference, Proceedings*, Vol. 2756 of Lecture Notes in Computer Science (Springer-Verlag, 2003), pp. 98–106.
17. H. Ragheb and E. R. Hancock, "Rough surface estimation using the Kirchhoff model," in *Image Analysis, Proceedings*, Vol. 2749 of Lecture Notes in Computer Science (Springer-Verlag, 2003), pp. 477–484.
18. T. M. Elfouhaily and C. A. Guerin, "A critical survey of approximate scattering wave theories from random rough surfaces," Waves Random Media **14**, R1–R40 (2004).
19. J. E. Harvey, C. L. Vernold, A. Krywonos, and P. L. Thompson, "Diffracted radiance: a fundamental quantity in a non-paraxial scalar diffraction theory," Appl. Opt. **38**, 6469–6481 (1999).
20. J. E. Harvey, C. L. Vernold, A. Krywonos, and P. L. Thompson, "Diffracted radiance: a fundamental quantity in a nonparaxial scalar diffraction theory: errata," Appl. Opt. **39**, 6374–6375 (2000).
21. J. E. Harvey, A. Krywonos, and Dijana Bogunovic, "Non-paraxial scalar treatment of sinusoidal phase gratings," J. Opt. Soc. Am. A **23**, 858–865 (2006).
22. R. J. Noll, "Effect of mid and high spatial frequencies on optical performance," Opt. Eng. **18**, 137–142 (1979).
23. J. E. Harvey, "Bridging the gap between "figure" and "finish"," presented at the Optical Society of America Optical Fabrication and Testing Meeting, Boston, Massachusetts, May 3, 1996.
24. E. L. Church, "Fractal surface finish," Appl. Opt. **27**, 1518–1526 (1988).
25. J. C. Stover, *Optical Scattering, Measurement and Analysis*, 2nd ed. (SPIE, 1995).
26. J. E. Harvey, N. Choi, A. Krywonos, S. Schroder, and D. H. Penalver, "Scattering from moderately rough interfaces between two arbitrary media," Proc. SPIE **7794**, 77940V (2010).
27. E. L. Church and P. Z. Takacs, "Instrumental effects in surface finish measurements," Proc. SPIE **1009**, 46–55 (1988).
28. E. L. Church and P. Z. Takacs, "Effects of the optical transfer function in surface profile measurements," Proc. SPIE **1164**, 46–59 (1989).
29. A. Duparré, J. Ferre-Borrull, S. Gliech, G. Notni, J. Steinert, and J. M. Bennett, "Surface characterization techniques for determining the root-mean-square roughness and power spectral densities of optical components," Appl. Opt. **41**, 154–171 (2002).
30. F. E. Nicodemus, "Reflectance nomenclature and directional reflectance and emissivity," Appl. Opt. **9**, 1474–1475 (1970).
31. J. E. Harvey, "Scattering effects in x-ray imaging systems," Proc. SPIE **2515**, 246–272 (1995).
32. A. Krywonos, "Predicting surface scatter using a linear systems formulation of nonparaxial scalar diffraction," Ph.D. dissertation (University of Central Florida, 2006).
33. J. A. Ratcliff, "Some aspects of diffraction theory and their application to the ionosphere," in *Reports of Progress in Physics*, A. C. Strickland, ed. (The Physical Society, 1956), Vol. XIX.
34. J. W. Goodman, *Introduction to Fourier Optics*, 2nd ed. (McGraw-Hill, 1996).
35. J. D. Gaskill, *Linear Systems, Fourier Transforms, and Optics* (Wiley, 1978).
36. J. E. Harvey and C. L. Vernold, "Description of diffraction grating behavior in direction cosine space," Appl. Opt. **37**, 8158–8160 (1998).
37. J. E. Harvey and A. Krywonos, "Radiance: the natural quantity for describing diffraction and propagation," Proc. SPIE **6285**, 628503 (2006).
38. Users Manual for APART/PADE, Version 8.6 (Breault Research Organization, 4601 East First Street, Tucson, Ariz., 1987), p. 5-2.
39. ASAP Reference Manual (Breault Research Organization, 4601 East First Street, Tucson, Ariz., 1990), pp. 3–43.
40. TracePro User's Manual, Release 3.0 (Lambda Research Corporation, 80 Taylor Street, Littleton, Mass. (1998), p. 7.12.
41. ZEMAX User's Guide, August 2007 (ZEMAX Development Corp., 3001 112th Avenue NE, Suite 202, Bellevue, Wash., 2007), p. 391.
42. FRED User's Manual, Version 9.110 (Photon Engineering, 440 S. Williams Blvd. #106, Tucson, Ariz., 2010).
43. http://www.opticsinfobase.org/submit/ocis/.
44. J. E. Harvey, E. C. Moran, and W. P. Zmek, "Transfer function characterization of grazing incidence optical systems," Appl. Opt. **27**, 1527–1533 (1988).
45. P. Glenn, P. Reid, A. Slomba, and L. P. Van Speybroeck, "Performance prediction of AXAF technology mirror assembly using measured mirror surface errors," Appl. Opt. **27**, 1539–1543 (1988).
46. J. E. Harvey and P. L. Thompson, "Generalized Wolter Type I design for the solar x-ray imager (SXI)," Proc. SPIE **3766**, 173–183 (1999).
47. J. E. Harvey, A. Krywonos, G. Peterson, and M. Bruner, "Image Degradation due to scattering effects in two-mirror telescopes," Opt. Eng. **49**, 063202 (2010).
48. H. Davies, "The reflection of electromagnetic waves from a rough surface," Proc. IEE IV **101**, 209–214 (1954).
49. H. E. Bennett and J. O. Porteus, "Relation between surface roughness and specular reflectance at normal incidence," J. Opt. Soc. Am. **51**, 123–129 (1961).

50. J. M. Bennett and L. Mattsson, *Introduction to Surface Roughness and Scattering* (Optical Society of America, 1989).
51. B. E. A. Saleh and M. C. Teich, *Fundamentals of Photonics* (Wiley, 1991).
52. S. Fay, S. Dubail, U. Kroll, J. Meier, Y. Ziegler, and A. Shah, "Light trapping enhancement for thin-film silicon solar cells by roughness improvement of the ZnC front TCO," in *Proceedings of the 16th European Photovoltaic Solar Energy Conference & Exhibition* (WIP Wirtschaft und Infrastruktur Planungs-KG, 2000), pp. 361–364.
53. D. Domine, F. J. Haug, C. Battaglia, and C. Ballif, "Modeling of light scattering from micro- and nanotextured surfaces," J. Appl. Phys. **107**, 044504 (2010).
54. S. Schröder, A. Duparré, K. Füchsel, N. Kaiser, A. Tünnermann, and J. E. Harvey, "Scattering of roughened TCO films—modeling and measurement," in *OSA Topical Meeting on Optical Interference Coatings*, OSA Technical Digest (CD) (2010).
55. M. Guzar-Sicairos and J. C. Gutierrez-Vega, "Computation of quasi-discrete Hankel transforms of integer order for propagating optical wave fields," J. Opt. Soc. Am. A **21**, 53–58 (2004).
56. K. A. O'Donnell and E. R. Mendez, "Experimental study of scattering from characterized random surfaces," J. Opt. Soc. Am. A **4**, 1194–1205 (1987).
57. E. L. Church and P. Z. Takacs, "The optimal estimation of finish parameters," Proc SPIE **1530**, 71–86 (1991).
58. J. M. Elson, J. M. Bennett, and J. C. Stover, "Wavelength and Angular Dependence of light scattering from beryllium: comparison of theory and experiment," Appl. Opt. **32**, 3362–3376 (1993).
59. M. G. Dittman, "*K*-correlation power spectral density and surface scatter model," Proc. SPIE **6291**, 62910P (2006).
60. A. J. S. Hamilton, "Uncorrelated modes of nonlinear power spectrum," Mon. Not. R. Astron. Soc. **312**, 257–284 (2000).
61. J. E. Harvey, N. Choi, A. Krywonos, and J. Marcen, "Calculating BRDFs from surface PSDs for moderately rough optical surfaces," Proc. SPIE **7426**, 742601 (2009).
62. J. C. Stover and J. E. Harvey, "Limitations of Rayleigh-Rice perturbation theory for describing surface scatter," Proc. SPIE **6672**, 66720B (2007).
63. J. E. Harvey, A. Krywonos, and J. C. Stover "Unified scatter model for rough surfaces at large incident and scatter angles," Proc. SPIE **6672**, 66720C (2007).
64. R. W. Boyd, *Radiometry and the Detection of Optical Radiation* (Wiley, 1983).
65. J. J. Murrey, F. E. Nicodemus, and I. Wunderman, "Proposed supplement to the SI nomenclature for radiometry and photometry," Appl. Opt. **10**, 1465–1468 (1971).
66. The NIST Reference on Constants, Units, and Uncertainty, http://physics.nist.gov/cuu/Units/units.html.
67. S. Schröder, S. Gliech, and A. Duparre, "Measurement system to determine the total and angle-resolved light scattering of optical components in the deep-ultraviolet and vacuum-ultraviolet spectral regions," Appl. Opt. **44**, 6093–6107 (2005).
68. E. L. Church, P. Z. Takacs, and T. A. Leonard, "The prediction of BRDFs from surface profile measurements," Proc. SPIE **1165**, 136–150 (1989).
69. S. Schröder, "Light scattering of optical components at 193 nm and 13.5 nm," Ph.D. dissertation (Friedrich-Schiller-Universitat, Jena, Germany, 2008).